Joint Centre for Mesoscale Meteorology, Reading, UK

Convective destabilisation by a tropopause fold diagnosed using potential vorticity inversion

K. Browning
A. J. Thorpe
M. Griffiths

Internal Report No. 96

October 1998

Met Office Joint Centre for Mesoscale Meteorology Department of Meteorology
University of Reading PO Box 243 Reading RG6 6BB United Kingdom
Tel: +44 (0)118 931 8425 Fax: +44 (0)118 931 8791
www.metoffice.com

Designed and produced by the Met Office © Crown copyright 2001 01/0240 The Met Office logo is a registered trademark.

Convective destabilisation by a tropopause fold diagnosed using potential vorticity inversion

Morwenna Griffiths[1], Alan Thorpe and Keith Browning

Summary

There is observational evidence to suggest that at the time tropopause folds in extra-tropical cyclones are descending into the mid troposphere there is frequently a destabilisation of the lower troposphere to moist convection. Here we consider the dynamical reasons for such a linkage using so-called potential vorticity (PV) attribution concepts. In particular a method is described using PV inversion to find the wind shear attributable to the tropopause fold itself. Then this shear is used to quantify the tendency to generate regions of potential instability, *i.e.* where the wet-bulb potential temperature decreases with height. The method is applied to a case of a modest tropopause fold and it is found that the potential vorticity anomaly contained in the tropopause fold can contribute susbtantially to the instantaneous convective destabilisation. Indeed, at some locations, it can overcome a tendency to stabilise by the atmosphere without the fold.

1 Introduction

Observational studies (see for example Uccellini (1990)) have shown that the tropopause is lowered in the region above a synoptic scale low pressure system. Browning (1996 and 1997) hypothesised that there is a causal connection between the lowered tropopause and convection, via differential advection of wet-bulb potential temperature. The dynamical role of the tropopause can be determined using potential vorticity (PV) concepts. For example, theoretical studies, such as Hoskins *et al.* (1985), show that the static stability is decreased below a positive upper-level potential vorticity anomaly. This does not, in itself, lead to potential instability, but it leaves the region more susceptible to the generation of potential instability. The aim of this study is to bring together such observations and PV ideas and to establish a dynamical link between the lowered tropopause and the destabilisation of the atmosphere. Specifically, we aim to provide a method for the quantification of the role of the tropopause fold in the development of potential instability and subsequent convection using potential vorticity. We show that the tropopause fold acts to increase the generation of potential instability in its vicinity.

Typically convection takes place in a region which is potentially unstable and subject to large-scale ascent. In this paper we investigate the generation and to a lesser extent the release of potential instability. Potential instability is present in an otherwise stable

[1]Corresponding author: Department of Meteorology, University of Reading, P.O. Box 243, Whiteknights, Reading, Berkshire, RG6 6BB, UK.

layer if forced ascent of that layer would cause it to become unstable. Note that it is important that the whole layer is raised. For static stability one considers raising a *parcel* of air in a stationary environment; this is different from raising a *layer* of air. The conditions for potential instability (also known as layer or convective instability) occur when the wet-bulb potential temperatue (θ_w) decreases with height; *i.e.* $\frac{\partial \theta_w}{\partial z} < 0$. This condition usually occurs when dry air overlays moist air. This potential instability will be realised as convection if sufficient forced ascent occurs. Following the ideas put forward by Browning *et al.* (1996), the layer from $900mb$ to $700mb$ is considered. Vertical shear in the horizontal wind is assumed in Browning *et al.* (1996) to cause wet-bulb potential temperature surfaces to be differentially advected leading to "over-running" of lower-θ_w air over higher-θ_w air. In this work we explore these ideas further and look at the wind attributable to different parts of the PV field to find out their effect on the creation of potential instability.

Potential vorticity has the useful property that, subject to a balance condition and boundary conditions, it is invertible - *i.e.* the wind and temperature field associated with a PV field can be determined. It has been suggested (Bishop and Thorpe, 1994) that the PV of the atmosphere can be separated into the sum of a set of potential vorticity anomalies, each with its own temperature and circulation. It is important to remember that temperature gradients on horizontal boundaries can be thought of as surrogate PV anomalies and as such are as important as the internal potential vorticity structure. For this theoretical discussion, the tropopause location after removal of the fold can be considered as the top boundary because the high values of PV in the stratosphere mean that information does not propagate far into the stratosphere. The existence of wind shear within the troposphere is then seen as action-at-a-distance by these PV anomalies, both surrogate and real.

A schematic diagram of a tropopause fold is shown in Figure 1. This shows an idealised east-west cross-section through a sloping frontal zone and tropopause fold. The solid crosses and dots indicate the flow associated with the tropopause fold. Note that this circulation decreases away from the fold. The flow associated with the upper-level temperature gradient, along the tropopause after removal of the fold, is marked by open crosses; again note that this decreases away from the upper boundary. The flow due to the lower boundary is in the opposite direction to that due to the upper boundary and is marked with open circles. The wind due to the upper boundary acts in such a way as to enhance the vertical shear due to the thermal gradient on the lower boundary. It is clear that the temperature gradient on the tropopause and at the surface, when viewed as surrogate PV anomalies, will have a significant effect on the winds in the troposphere as shown in Figure 1. It is the aim of this study to investigate the *additional* effect of the lowered tropopause. The inversion of potential vorticity is used here to determine the circulation associated with different parts of the field of PV. In particular, the circulation associated with the tropopause fold is found and its effect on the destabilisation of the the atmosphere is quantified. We do not explicitly calculate the wind due to the surrogate PV anomalies.

Thorpe (1997) has discussed the vertical motion attributable to a tropopause fold. We

show here that the vertical velocity (and its associated horizontal divergent wind) cannot be neglected when calculating the *generation* of potential instability. In addition forced ascent is required for the *release* of the potential instability; this ascent is not always present and so not all the potential instability is realised. Also note the regions of convective rain will be adjacent to but not co-incident with the regions of potential instability because in these regions the potential instability has been realised to make the convective rain.

This study first gives an outline of the method used and its differences from similar methods used by previous authors and highlights the implications of these differences. As an example the method is applied to a mid-latitude low pressure system that passed over the UK in May 1995. This case has been chosen not because it is an example of a particularly intense tropopause fold, but because the system is slow moving and remained within the domain of the mesoscale version of the UK Meteorological Office (UKMO) Unified model for the period of interest. This system has been studied by Browning *et al.* (1996) using water vapour (WV) imagery and the UKMO's limited area version of the Unified Model with a 50km resolution (LAM). They observed convection/thunderstorms near the region of dry WV and high potential vorticity and were able to explain this qualitatively in terms of differential advection of the θ_w surfaces. Here we shall extend their ideas and attempt to assess quantitatively the extent to which differential advection of these θ_w surfaces can be attributed to the lowered tropopause by using piecewise PV inversion. This study uses the mesoscale version of the UKMO Unified Model which has a horizontal resolution of 17km and 31 levels in the vertical; see Cullen (1993) for a full description of the Unified Model.

This paper is structured as follows: in section 2 the theory of the generation of potential instability is described. In section 3 the method to find wind and temperaure using PV inversion is described. This theory and method are then applied to a case study in section 4.

2 Dynamical theory of convective destabilisation

In this section the generation of convective instability is investigated. As stated earlier potential instability is concerned with the gradient of θ_w with height. Changes in the vertical gradient of θ_w depend on the movement/reorientation of θ_w surfaces. There are three possible mechanisms for the movement of θ_w surfaces. These are (a) diabatic processes, (b) advection by the divergent wind, and (c) advection by the non-divergent wind (as implied by inversion of the PV distribution). In this paper, estimates of the size of (b) and (c) are made. In our case study, (a) is determined to be small by using trajectory analysis and is therefore neglected.

2.1 Generation of potential instability

The generation of potential instability is central to this study. A quantitative way to measure this is to quantify the rate of change of $\frac{\partial \theta_w}{\partial z}$ following a parcel *i.e.* $\frac{D}{Dt}\left(\frac{\partial \theta_w}{\partial z}\right)$. Expanding this gives

$$\frac{D}{Dt}\left(\frac{\partial \theta_w}{\partial z}\right) = \frac{\partial}{\partial z}\left(\frac{D\theta_w}{Dt}\right) - \frac{\partial \mathbf{u}}{\partial z}.\nabla\theta_w, \tag{1}$$

where $\mathbf{u}$ has both horizontal and vertical components[2]. In the absence of friction or precipitation, θ_w is conserved and so

$$\frac{D}{Dt}\left(\frac{\partial \theta_w}{\partial z}\right) = -\frac{\partial \mathbf{u}}{\partial z}.\nabla\theta_w. \tag{2}$$

If the wind is in thermal wind balance, it can be shown that

$$\frac{D}{Dt}\left(\frac{\partial \theta_w}{\partial z}\right) = -\frac{g}{f\theta_o}\mathbf{k}.\nabla\theta \times \nabla\theta_w. \tag{3}$$

Equation (3) indicates that there is a non-zero tendency of $\partial\theta_w/\partial z$ if the iso-contours of θ and θ_w are not congruent. This will happen only in a moist atmosphere where there is a humidity gradient along isentropic surfaces. The generation of potential instability is favoured if, in the direction of the thermal wind, there is relatively moist air downstream and relatively dry air upstream of the thermal wind. Figure (2) shows this situation.

Returning to equation (2) we see that the generation of potential instability is favoured if there is a positive component of the wind shear vector in the direction of the vector gradient of θ_w. For example, consider the case of a purely horizontal flow. Imagine, as is typical, $\partial\theta_w/\partial z > 0$ in the presence of a horizontal θ_w gradient. Hence the θ_w contours will slope in the vertical. Then the generation term given in equation (2) implies that the generation of potential instability is favoured if θ_w contours are differentially advected at various levels in a way such that air with lower θ_w at upper levels "over-runs" air with higher θ_w at lower levels; see lower panel in Figure (2). Note however that the expression "over-running" does not fully account for every aspect of the generation term in equation (2). For example, vertical motion can alter $\partial\theta_w/\partial z$ in certain circumstances *but it cannot give rise to negative stability.*

As stated in the introduction, there will be a contribution to the destabilisation of the troposphere due to temperature gradients on the horizontal boundaries. Even if the tropopause is not folded but still exhibits a temperature gradient along it, it will act in a similar way to the folded tropopause in inducing remotely a wind shear. In this study we seek to determine only the *additional* contribution to the wind shear due to the folded PV structure of the tropopause. The importance of assessing the additional contribution due to folds is that the small horizontal scale of these folds will focus and amplify any convective destabilisation locally. Current NWP models probably do not handle these small scales very accurately.

[2]the convention used in this paper is that $\mathbf{v}$ is used to represent a two-dimensional wind and $\mathbf{u}$ is used for three dimensional winds.

The wind, $\mathbf{u}$, can be separated, using PV inversion (described in Section 3), into that attributable to the "flat" tropopause (denoted by an overbar) and that attributable to the fold (denoted by a prime) in the way outlined below. The PV structure of the "flat" tropopause is obtained by subtracting the fold PV anomaly from the full field; note that this leads to a more nearly horizontal tropopause, but not one that is perfectly flat. Equation (2) can be written as

$$\frac{D}{Dt}\left(\frac{\partial \theta_w}{\partial z}\right) = -\frac{\partial \overline{\mathbf{u}}}{\partial z}.\nabla\theta_w - \frac{\partial \mathbf{u}'}{\partial z}.\nabla\theta_w \tag{4}$$

and the relative size of both terms on the right hand side of (4) can be estimated. The term $\frac{\partial \overline{\mathbf{u}}}{\partial z}.\nabla\theta_w$ represents destabilisation by the wind associated with the "flat tropopause", while the term $\frac{\partial \mathbf{u}'}{\partial z}.\nabla\theta_w$ represents destabilisation by the wind associated with the PV anomaly.

The partitioning given in equation (4) shows the effect of the wind attributable to different PV features advecting the *total* temperature field. It is clear that equation (4) could have been partitioned differently. For example, it would be possible to investigate the effect of the total wind advecting temperature gradients due to different PV features but this is not done here.

3 PV Inversion Methodology

In this section we describe the method used for determining the wind and temperature fields from the PV field.

3.1 PV Inversion: Non-Divergent Wind Calculation

Following the method used by Davis and Emanuel (1991), the potential vorticity is defined as:

$$PV = \frac{g\gamma\pi}{p}\left[(f+\nabla^2\Psi)\Phi_{\pi\pi} - \frac{1}{a^2\cos^2\phi}\Psi_{\lambda\pi}\Phi_{\lambda\pi} - \frac{1}{a^2}\Psi_{\phi\pi}\Phi_{\phi\pi}\right] \tag{5}$$

which is the full Ertel PV assuming non-divergence and hydrostatic balance. For this work, we use the Charney non-linear balance condition (Charney, 1955):

$$\nabla^2\Phi = \nabla.(f.\nabla\Psi) + \frac{2}{a^4\cos^2\phi}(\Psi_{\lambda\lambda}\Psi_{\phi\phi} - \Psi^2_{\lambda\phi}) \tag{6}$$

where Ψ is the streamfunction, Φ is the geopotential, λ is the longitude, ϕ is the latitude, π is the Exner pressure (defined as $c_p\left(\frac{p}{p_o}\right)^{\gamma}$, $p_o = 1000mb$), a is the radius of the earth and $\gamma = R_d/C_p$. The non-divergent wind associated with the PV distribution is then defined by $\mathbf{v_r} = (-\frac{\partial\Psi}{\partial\mathbf{y}}, \frac{\partial\Psi}{\partial\mathbf{x}})$. These equations are solved by creating a third equation ((5)-(6)), rearranging:

$$\begin{aligned}\nabla^2\Phi + c_1(f+\nabla^2\Psi)\Phi_{\pi\pi} &= c_2 PV \\ +c_1\left(\frac{1}{a^2\cos\phi}\Psi_{\lambda\pi}\Phi_{\lambda\pi} + \frac{1}{a^2}\Psi_{\phi\pi}\Phi_{\phi\pi}\right) \;+\; &\nabla(f\nabla\Psi) + \frac{2}{a^4\cos^2\phi}(\Psi_{\lambda\lambda}\Psi_{\phi\phi} - \Psi^2_{\phi\lambda})\end{aligned} \tag{7}$$

where $c_1 = \frac{H^2}{fL^2}\left(\frac{g}{\theta_o}\right)^2$, $c_2 = \frac{H^2}{fL^2}\left(\frac{g}{\theta_o}\right)\frac{p}{g\gamma\pi}$, f is the Coriolis parameter, $\theta_o = 300K$ is a reference temperature and H and L are representative length scales in the vertical and horizontal respectively. For this work, $H = 10km$ and $L = 2000km$ provide the best convergence rate for the numerical algorithm.

The Charney non-linear balance equation is rearranged to give a two dimensional equation for Ψ:

$$\nabla^2\Psi = \frac{1}{f}\left(\nabla^2\Phi - \nabla f\nabla\Psi - \frac{2}{a^4\cos^2\phi}(\Psi_{\lambda\lambda}\Psi_{\phi\phi} - \Psi^2_{\lambda\phi})\right) \tag{8}$$

Equations (7) and (8) are solved iteratively to obtain a (Φ, Ψ) pair. The iterative process is considered to be complete when the PV calculated from (5) is within 0.05PVU of the analysed PV at every point, and the maximum error in (8) is less than $0.05f$ at each point.

The boundary conditions used for solving eqation (8) are the same as those used by Davis and Emanuel (1991) *i.e.* Ψ is defined so that the total divergence is zero on each level as follows:

$$\frac{\partial\Psi}{\partial s} = -\mathbf{v}.\mathbf{n} + \frac{\oint \mathbf{v}.\mathbf{n}dl}{\oint dl}. \tag{9}$$

where $\mathbf{s}$ is the unit vector parallel to the boundary and $\mathbf{n}$ is the unit vector normal to the boundary. In order to solve consistently this pair of equations, fPV should be positive everywhere, so for the Northern Hemisphere, we choose to set $PV > 0.02PVU$ everywhere.

The lateral boundary conditions for solving equation (7) are the same as those used by Davis and Emanuel (1991); *i.e.* hydrostatic balance is assumed. However, the horizontal boundary conditions used are different. As this is an elliptic equation, on the horizontal boundaries (at 900mb and 50mb) we can choose to use either Neumann (Φ_π specified) or Dirichlet (Φ specified) boundary conditions (Press *et al.*, 1992). When inverting the total PV field, it makes very little difference whether the Neumann or Dirichlet conditions are used. Most authors in the past have used the Neumann condition. For this work we are interested in the wind shear associated with the PV anomalies and have chosen to use Dirichlet conditions to find an upper bound on the wind shear. The Neumann condition gives a lower bound and is mentioned briefly at the end of the paper.

In order to isolate the effect of the tropopause fold, first the wind and temperature fields associated with the full (model) PV are calculated. Then the wind and temperature fields associated with the PV distribution with the fold removed are found. This will be referred to as the 'flat tropopause case', although it is clear that the remaining tropopause is not completely horizontal. These fields are subtracted to give the wind and temperature attributable to the PV fold. It should be noted that the fields attributed to the fold calculated in this way depend strongly on the surrounding PV distribution as is physically expected. The region from 900mb to 50mb has been chosen for the PV inversion in order to avoid boundary layer effects. Therefore the surrogate PV anomaly at the "surface" will here refer to the 900mb level.

3.2 PV Inversion: Divergent Wind Calculation

The PV inversion of the previous section gives the non-divergent wind field associated with the PV distribution. The wind, $\mathbf{u}$, in equation (4) includes both divergent and non-divergent components. This section describes how the divergent component is calculated. Usually the divergent component of the wind is diagnosed as a residual after calculating the rotational (non-divergent) component. This works well when one is interested in separating the total wind into components. However, for attribution studies such as this one, it is not possible to use the residual since we do not know the full wind for the case of the "flat" tropopause. Instead, we have chosen to use the quasi-geostrophic approximation in order to find the vertical velocity. In particular, we use the quasi-geostrophic omega equation Bluestein (1992):

$$\sigma^2 \nabla_h^2 \omega + f^2 \frac{\partial^2 \omega}{\partial p^2} = -2\nabla.\mathbf{Q} \tag{10}$$

where

$$\mathbf{Q} = \left(-\frac{r}{p} \frac{1}{a\cos\phi} \frac{\partial \mathbf{v}}{\partial \lambda}.\nabla T, -\frac{r}{p} \frac{1}{a} \frac{\partial \mathbf{v}}{\partial \phi}.\nabla T \right) \tag{11}$$

$$\sigma^2 = \frac{-1}{\bar{\rho}\bar{\theta}} \left(\frac{\partial \bar{\theta}}{\partial p} \right) \tag{12}$$

Equation (10) is solved with $\omega = 0$ on the top and bottom boundaries. Once ω $(= \frac{Dp}{Dt})$ has been found, the horizontal components of the divergent wind (u_d, v_d) are determined by defining a velocity potential (χ) such that

$$(u_d, v_d) = \left(\frac{1}{a\cos\phi} \frac{\partial \chi}{\partial \lambda}, \frac{1}{a} \frac{\partial \chi}{\partial \phi} \right)$$

and finding χ from the continuity equation

$$\nabla^2 \chi = -\frac{\partial \omega}{\partial p}. \tag{13}$$

In solving equation (13) there is a choice of boundary conditions. Either Dirichlet conditions can be used to specify that the total rotation associated with the divergent flow to be zero, or Neumann conditions can be used to specify the total divergence. For the calculation of the divergent flow Dirichlet conditions are used *i.e.*,

$$\frac{\partial \chi}{\partial s} = \mathbf{v}'.\mathbf{s} - \frac{\oint \mathbf{v}'.\mathbf{s} dl}{\oint dl} \tag{14}$$

where $\mathbf{v}'$ is the difference between the original (model) wind and the wind obtained from PV inversion ($\mathbf{v}' = \mathbf{v} - \mathbf{v_r}$) and $\mathbf{s}$ is the unit vector parallel to the boundary. Note the similarity between this boundary condition on χ and the boundary condition used for Ψ defined by equation (9). As mentioned other boundary conditions could be used to obtain a solution consistent with equation (13). However, this chosen boundary condition gives a divergent wind close to, but not exactly the same as, $\mathbf{v}'$. Diabatic effects were neglected in equation (10), and $\mathbf{v}'$ has both a rotational component and an unbalanced (gravity wave) component.

This calculation is carried out for the case with no change to the PV and for the "flat" tropopause case. These are then subtracted to obtain the divergent wind associated with the fold.

4 Convective destabilisation on 17 May 1995

4.1 Meteorological situation

In this section a brief overview of the meteorological situation is given and it is not intended to be an exhaustive study of the event. It is based on a forecast of the UKMO mesoscale model run forward from 0Z 17/5/95.

Figure 3 shows the mean sea level pressure at 6 hourly intervals for the period of interest. This discussion starts at 0Z 17/5/95, at which stage there is very little potential instability (shaded in Figure 3) and none associated with the system of interest. At the initial time there is a broad low-pressure system over southern England and extending into France, with two centres. The centre of interest (labelled L) is over Cornwall. At this time it has a central mean-sea-level pressure of just under 1000mb. It has almost no PV signature at the surface, and not much at upper levels. At upper levels there is a broad band of slightly lowered stratospheric air (450-500mb) extending in a NE-SW direction over northern Scotland and Ireland.

Figure 4 shows the evolution of the upper-level PV anomaly in terms of the 1.5PVU contour on 550mb at 6Z, 12Z and 18Z. This shows that the region of relatively high-PV air extends over a broader region as the system evolves. At 6Z there is a little PV signature southwest of Ireland which grows and extends over south-western England by 12Z. The 2PVU surface comes down to about 550-600mb at this time.

At 12Z the low pressure centre had deepened to about 996mb and moved north-east. A region of potential instability was present south of the low, over south-east England and the English channel (Figure 3). The model's region of convective rain (not shown) spanned the area over the channel between England and western Belgium. There was large scale (dynamic) rain in the model along the coast to the north of the centre of the low. The tropopause fold at this time was situated to the west of the low. Figure 5 shows a roughly north-south section through (6W,48N) (6W,60N) and clearly shows the sloping θ_w front as well as the lowered and folded tropopause. There was very little θ signature (not shown). The region in which the relative humidity is less than 30% is shaded; note the dry stratospheric air extending along the tropopause fold. There was a broad region of ascent on the warm side of the lowered tropopause, and a region of descent in the region of the lowered tropopause (as inferred by looking at 500mb) (not shown). At this stage the upper-level (PV=2PVU) air extended down to 560 mb to the southwest of the surface low, and there was a significant PV anomaly (1.5PVU) developing near the surface (and up to about 700mb) probably as a result of the onset of latent heat release (not shown).

The upper and lower-level anomalies were quite distinct from one another with the lower one being centred just to the west of the surface low, and the upper one approximately 200km to the southwest.

At 18Z the surface low pressure centre had moved to the northeast, and deepened to 991mb (Figure 3). The region of greatest potential instability was to the east and southeast of the surface low and the region of maximum convective rain was over it and to the north. The dry intrusion surrounding the tropopause fold extended downwards and to the south, with upward motion in the warm air ahead of it and downward motion in the cold air behind - a thermally direct circulation. As at 12Z there was an upper θ_w front associated with the tropopause fold, but this appeared to have weakened. The PV anomaly extending downwards from the stratosphere had become stronger, with 2PVU air reaching down to 600mb. At this time the low-level PV anomaly was also becoming stronger, with 1.5PVU air reaching as high as 650mb. The low-level anomaly continued to be distinct from the upper one. The upper anomaly sloped downwards to the south while the lower one extended almost vertically up from near the surface low pressure centre.

4.2 Comparison with a model of lower resolution

It is interesting to make a comparison between the 50km resolution UKMO Limited Area Model (LAM) used in the earlier study by Browning *et al.* (1996) and the 17km resolution mesoscale model used in this study. Figure 6 shows the same cross-section as Figure 5 but for the LAM. The same broad features can be identified in both cross-sections - an upper and lower θ_w front, a lowering of the tropopause associated with the upper front, and a layer of weak static stability beneath the lowered tropopause. However there is more fine structure in the higher resolution model. In particular it is interesting to note the downward extent of higher PV values in the mesoscale model: the 2PVU air descends to 600mb in the mesoscale model but only to almost 500mb in the LAM at 12Z. In the rest of this paper we exploit the mesoscale model because of its ability to better resolve the feature of interest.

4.3 Definition of the PV anomalies

The method described in section 3 is now applied to the case described in section 4.1 to assess the importance of the tropopause fold in destabilising the atmosphere. Figure 7 is a cross-section at about 8W through the PV fold at 6Z (the exact position is shown in Figure 9b). These and the following cross-sections are oriented north-south in order to highlight the two sub-regions of anomalous PV discussed below. The clear difference between the stratosphere and the troposphere can be seen in this diagram, with high PV air in the stratosphere and low PV air in the troposphere. Two anomalies are considered, one where the 2PVU surface descends to below 500mb, described here as 'the fold', marked F, and the other where there is relatively high PV air in the stratosphere (at around 300mb) marked S. The effect of each of these anomalies on the flow in the underlying

troposphere is discussed in the next section. Figure 8 shows the same cross-section as Figure 7 but with the fold removed. The fold was removed by defining a box[3] and altering the PV within that area by setting all values larger than 0.5PVU to 0.5PVU (a typical tropospheric value). Figure 9 is the difference between these two fields in Figures 7 and 8 and it shows the PV anomaly associated with the fold (F). Figure 9a is the same (vertical) cross-section as Figures 7 and 8, while Figure 9b is a horizontal section at 400mb and also shows the position of the sections in the previous figures. This definition of the fold is arbitrary but it is sufficient to illustrate the destabilisation due to the tropopause undulations.

The stratospheric PV anomaly (S) was removed by defining a box[4] which contained the PV anomaly and altering the PV within that box as follows:

at 300mb:	if PV > 6PVU then PV = 6PVU
at 250mb:	if PV > 8PVU then PV = 8PVU
at 200mb:	if PV > 9PVU then PV = 9PVU

This proceedure takes into account the change of the background stratospheric PV with height. All other values are unchanged. A vertical section through the stratospheric anomaly is shown in Figure 10.

4.4 Role of PV anomalies in destabilising the troposphere

4.4.1 The tendency to increase potential instability

In this section we look at the generation of potential instability due the PV anomalies defined above. We focus on the effect of the tropopause fold because, being lower, it has a greater effect in the lower troposphere. Recall that it is the vertical shear of the wind associated with the PV which destabilises the air when acting upon an appropriate θ_w field, (see equation (2)). To highlight the area of interest, only a sub-area of the mesoscale model domain is plotted in the following figures. The vectors in Figure 11a show the shear between 900mb and 700mb of the wind associated with the full PV field. Also plotted on Figure 11a are contours of θ_w at 800mb. The orientation of these contours and the vectors show that over a large region the shear vector has a component across the θ_w contours towards the high-θ_w air in such a way as to tend to destabilise the atmosphere; see equation (2). In Figure 11b we show contours of θ and θ_w at 800mb, this being an alternative way of visualising the destabilisation by using equation (3). In this case, we can ascertain whether the angle between the horizontal gradients of θ and θ_w is such as to reduce the vertical gradient of θ_w. Compare the orientation of isolines of θ and θ_w in

[3]bounded by the longitude, latitude pairs: (13.43W,49.72N), (15.87W,58.15N), (1.24E,58.75N), (.55E,50.21N) and between 650mb and 350mb in the vertical

[4]bounded by the longitude, latitude pairs: (15.2W,56.1), (3.0W,56.7), (2.9W,47.1), (12.7W,46.6) and between 300mb and 200mb in the vertical

Figure 11b and the idealised case shown in Figure 2. Note that there is a large region in which the tendency is towards destabilising the atmosphere.

Figure 11 has been included to enable us to visualise the parts of the terms on the right-hand side of equations (2) and (3). These terms can be calculated explicitly and this is done in the following figures. Contour plots showing (a) the total generation of potential instability (the right hand side of equation (2)) and (b) the generation of potential instability due to the flat tropopause alone (the first term on the right hand side of equation (3)) are given in Figure 12. Again, only a subsection of the domain is plotted to highlight the area of interest. In these plots the contributions due to the non-divergent and divergent components of the wind are combined. The contribution to $-\frac{\partial \mathbf{u}}{\partial z}.\nabla\theta_w$ due to the divergent wind (not explicitly shown) is in the opposite sense (but smaller) to that due to the rotational component. The thick closed contour over southwest England shows the region of minimum potential stability *i.e.* the zero contour of the difference between θ_w at 900mb and at 700mb. Note that in this region of minimum potential stability the tendency is for the lower troposphere to become even less stable.

Not only is it important to quantify the tendency for the atmosphere to become less stable ($\frac{D}{Dt}\frac{\partial\theta_w}{\partial z} < 0$) but also to show that this tendency is strong enough and lasts long enough actually to create potential instability ($\frac{\partial\theta_w}{\partial z} < 0$) where it does not already exisit. The previous discussion looks at the tendency to generate instability but does not investigate whether the potential instability actually arises. For example, if the atmosphere was initially very stable then even a large tendency towards destabilisation might not result in potential instability. The current potential stability (or otherwise) as determined by $\frac{\partial\theta_w}{\partial z}$ between 700 and 900mb is shown in Figure 13. This figure shows that the region with potential instability (enclosed by the bold line) is away from the tropopause fold but still within the region with negative stability tendency.

The generation of destabilisation not explained by internal PV structure can be explained in terms of the gradients of temperature on the horizontal boundaries (ie at the ground and at the tropopause). Figure 12b shows show that with the flat tropopause alone the tendency is towards destabilisation in some regions. Since most of the internal PV gradients have been removed, this tendency is due largely to the temperature gradients on the boundaries (surrogate PV anomalies). The vertical profile of the maximum of $|\nabla_h\theta|$ both for the situation where the PV includes the fold, and for when the PV fold has been removed is shown in Figure 14. These profiles have been constructed by examining each level independently to find the maximum $|\nabla_h\theta|$ on that level in the region shown in Figure 12. By allowing the (horizontal) position on $|\nabla_h\theta|$ to vary with height, we are able to take into account the fact that the frontal region slopes with height. It is clear from the profiles in Figure 14 that the upper maximum in horizontal temperature gradient is larger and closer to the ground when the PV fold is present, but that it still exists when the PV fold is removed. This explains why there is still destabilisation when the fold is removed. However, the change in the height and magnitude of the maximum explains why the destabilisation is larger when the fold is present. The existence of the fold lowers the level of maximum upper level baroclinicity from about 400-350mb to 500-450mb and hence lowers the region of large "induced" wind shear. Note that the surface temperature

gradient remains almost unchanged, because the PV was altered at upper levels and its effect diminishes with distance.

The contribution to the destabilisation associated with the fold-induced wind shear is shown in Figures 15 and 16. The vectors plotted in Figure 15 show the wind shear between 900mb and 700mb associated with the tropopause fold. This wind shear includes both the divergent and non-divergent winds. Note the expected cyclonic rotation of this wind shear, consistent with idealised studies of positive upper PV anomalies. The contours are the same as those plotted in Figure 11a. The shear vectors point across the 800mb θ_w contours from warm to cold air (as in Figure 11a) implying that the wind shear associated with the PV anomaly acts to destabilise the troposphere and contributes in a positive way to the total destabilisation implied by Figure 11a. Figure 16 shows contours of the second term on the right hand side of equation (4), $\frac{\partial \mathbf{u}'}{\partial z}.\nabla\theta_w$, revealing a pattern similar to that shown in Figure 12a but with a smaller amplitude away from the tropopause fold. This is consistent with action-at-a-distance ideas which indicate that the effect of the fold should decrease away from the fold. In summary, we can see that the effect of the fold is largest in the region where the troposphere is currently stable (at 6Z). In the region where the current stability is low and therefore destabilisation is likely to be more effective, there is still a small contribution to further destabilisation associated with the fold.

4.4.2 Availability of large scale ascent to release the potential instability

We have shown that the winds associated with the fold act to destabilise the lower troposphere. However, as stated earlier the link between the generation of potential instability and convection is not straightforward. First the generation of instability must act on air which is already not too stable (or act for a long time on more stable air) to create potential instability. Then this potential instability must be in a region of forced large scale ascent for it to be released and for convection to occur. We have investigated these issues by means of 12-hour trajectory analyses starting at 6Z. Trajectories are started from two regions as shown in Figure 17a. The more westerly of these regions was chosen because it is where the rate of destabilisation due to the fold is largest. The eastern region was chosen to give trajectories which *end* near the region of convection at 18Z. Coincidently, this is near the region of minumum stability at 6Z. The trajectories were calculated using the method described in Wernli and Davies (1997). Trajectories were started on model levels between 850mb and 750mb. The trajectories shown were obtained by averaging trajectories calculated forward from all points within the areas defined by the points at the start of the trajectories in Figure 17a. The average trajectories will be referred to as A and B. Trajectory A starts in the region where the destabilisation associated with the tropopause fold is largest, trajectory B starts in the region which is least potentially stable at 6Z and ends near the region of convection. The end points are marked and lie approximately along the frontal zone.

The change in the potential stability $\left(\frac{\partial \theta_w}{\partial z}\right)$ with time along these two trajectories is shown in Figure 17b. We see that, at the start, the air is more stable in the trajectory further west

as would be expected from looking at Figure 13. At the start, the rate of destabilisation, as indicated by the slope, is greater for trajectory A than for trajectory B. This is to be expected when looking at Figure 12 which shows the *total* generation of potential instability. The pressure along each of these trajectories is shown in Figure 17c, it can be seen that parcels on the A trajectory descend on average, while parcels on the B trajectory ascend. Recall that for the release of potential instability, vertical motion is required. This explains why parcels at the end of trajectory B have more convection associated with them than those of trajectory A despite there being more potential instability associated with trajectory A. Remember also that once the potential instability has been released and it has rained $\frac{\partial \theta_w}{\partial z}$ will become close to zero. This effect can be seen in trajectory B in Figure 17b.

4.4.3 Quantification of the relative importance of the PV anomalies in destabilising the atmosphere

We are interested in the contribution to the destabilisation by the winds associated with the tropopause fold. It is clear from the previous discussion that this contribution is variable and decreases away from the fold. For the particular time we have chosen the trajectory analysis shows that the largest contribution associated with the fold is in a region which does not then lead to convection. This is not to say that the fold in this case never contributes to the generation of convection: it is possible that at earlier or later times the fold plays a significant role in destabilising the atmosphere in a region which then leads to convection. The first three lines in Table 1 show the contribution to destabilisation at three points in the model domain. These points were chosen to highlight different features. The first point is where the contribution associated with the fold is a maximum, the second point is where the total rate of destabilisation is largest and the final point is within the region which eventually leads to convection. It is clear from this table that the tropopause fold can be associated with a significant contribution to the instantaneous generation of potential instability.

In section 4.3, two PV anomalies were defined, the tropopause fold (F) and a stratospheric anomaly (S). In the analysis presented so far attention has been focussed on the tropopause fold. Here we look briefly at the stratospheric anomaly. The maximum contribution of the stratospheric anomaly to the generation of potential instability is shown in the fourth line in Table 1. The contribution to the generation of instability associated with the stratospheric anomaly is evidently very much smaller than that due to the tropopause fold. The reason for this is two-fold. Firstly it is further away from the lower troposphere, so action-at-a-distance ideas indicate that it should have less effect. Clough *et al.* (1996) discuss action-at-a-distance ideas. Secondly, unlike the tropopause fold, it does not focus and lower the upper-level temperature gradient.

So far all the results have been based on calculations using the Dirichlet boundary condidition when solving Equation (7). For comparison, the last row in Table 1 shows the values due to the tropopause fold when the Neumann boundary condition is used The

Neumann condition, by its definition, implies less wind shear near the boundaries and so the generation of instability in the way defined here is forced to be smaller. Partitioning the atmosphere into a sum of potential vorticity anomalies requires due consideration of the boundary temperature gradients and the two results presented here give an upper and lower bound on the contribution due to the internal PV structure.

5 Conclusions

In this paper a method is given to attribute, to different PV anomalies, the generation of potential instability by differential advection of a gradient of θ_w. This method is applied to a case in which there was a moderate amount of convection in the region of a well defined but small tropopause fold associated with a low pressure system passing over the UK.

PV inversion and attribution ideas have been used to show that the tropopause fold can make a large contribution to the differential wrapping up of θ_w surfaces and consequent potential destabilisation of the atmosphere. In this particular case we have shown that the tropopause fold contributed significantly to the generation of potential instability. Indeed, in some regions, it even acted to overcome a large scale tendency for stabilisation. At the time investigated in this study, there was a modest contribution to the destabilisation associated with the fold in the region which led to convection. In the region of maximum contribution by the tropopause fold to the destabilisation there was large scale descent and so the potential instability was not realised. From a single case study such as this one, there is no way of knowing if this is the general rule, or specific just to this case. It may be the case that in other storms the tropopause fold plays an important role in generating potential instability which then leads to convection.

There are many complicated processes going on in a full numerical model that can obscure our understanding of the simpler, more basic processes. These thoughts lead to two interesting extensions to this work. The first would be to do a similar study on a large number of mid-latitude cyclones, and the other would be to do a similar study on an idealised 'generic' mid-latitude cyclone. Both these studies would help to build a conceptual model of a developing mid-latitude cylone including the role of the tropopause fold.

6 Acknowledgement

Thanks are due to Michal Ziemianski for an early version of the PV inversion code. The authors acknowledge receipt of a NERC grant GR3/10204 supporting this research. Help with the graphics and the use of the Unified Model has been obtained through the NERC-supported UWERN programme.

7 References

Bishop, C. H. and Thorpe, A. J. (1994). Potential vorticity and the electrostatics analogy: Quasi-geostrophic theory. *Quart. J. Roy. Meteor. Soc.*, **120**, 713–731.

Bluestein, H. B. (1992). *Synoptic-Dynamic Meteorology in the midlatitudes. Volume 1 Principles of kinematics and dynamics.* Oxford University Press.

Browning, K. A., Roberts, N. M., and Sim, C. S. (1996). A mesoscale vortex diagnosed from combined satellite and model data. *Meteorol. Appl.*, **3**, 1–4.

Browning, K. A., Ballard, S. P., and Davitt, C. S. A. (1997). High-resolution analysis of frontal fracture. *Mon. Wea. Rev.*, **125**, 1212–1230.

Charney, J. G. (1955). The use of the primitive equations of motion in numerical prediction. *Tellus*, **7**, 22–26.

Clough, S. A., Davitt, C. S. A., and Thorpe, A. J. (1996). Attribution concepts applied to the omega equation. *Quart. J. Roy. Meteor. Soc.*, **122**, 1943–1962.

Cullen, M. J. P. (1993). The unified forecast climate model. *Meteorological Magazine*, **122**, 81–94.

Davis, C. A. and Emanuel, K. A. (1991). Potential vorticity diagnostics of cyclogenesis. *Mon. Wea. Rev.*, **119**, 1929–1953.

Hoskins, B. J., McIntyre, M. E., and Robertson, A. W. (1985). On the use and significance of isentropic potential vorticity maps. *Quart. J. Roy. Meteor. Soc.*, **111**, 877–946.

Press, W. H., Teukolsky, S. A., Vetterling, W. T., and Flannery, B. P. (1992). *Numerical Recipes in FORTRAN.* Cambridge University Press.

Thorpe, A. J. (1997). Attribution and its application to the mesoscale structure associated with tropopause folds. *Quart. J. Roy. Meteor. Soc.*, **123**, 2377–2399.

Uccellini, L. W. (1990). Processes contributing to the rapid development of extra-tropical cyclones. In C. W. Newton and E. O. Holopainen, editors, *Extratropical Cyclones. The Erik Palmen Memorial Volume*, pages 81–105. American Meteorological Society.

Wernli, H. and Davies, H. C. (1997). A lagrangian-based analysis of extratropical cyclones. I: the method and some applications. *Quart. J. Roy. Meteor. Soc.*, **123**, 467–490.

List of Figures

1 Schematic diagram of a tropopause fold (thick line) and frontal zone (thin lines) showing the contribution to the wind in the troposphere associated with three features - the PV fold (indicated by shading), the temperature gradient on the upper boundary (indicated by the upper thin horizontal line) and the temperature gradient on the lower boundary. The strength of the flow is proportional to the size of the symbols. . . . . .

2 Diagram showing configuration of θ and θ_w with associated wind and moisture fields which gives rise to the generation of potential instability. In (a) a horizontal section is shown, the solid lines denote contours of θ_w, the dashed lines show θ, the vector denotes the direction of the thermal wind. In (b) a vertical section is shown; again the solid lines indicate θ_w and the vectors show the thermal wind. Vector representations of the terms on the right-hand sides of equations (3) and (2) are shown on the right hand sides of diagrams (a) and (b) respectively. . . . . .

3 The mean sea level pressure from 0Z to 18Z. The contour interval is 2 mb. The shaded regions show regions of significant potential instability, *i.e.* where $\theta_w(700mb) - \theta_w(900mb) < -0.5K$ . . . . . .

4 Contours showing the evolution of the lowered tropopause. Contours are 1.5PVU on the 550mb surface at 6,12 and 18Z. The region inside the contour at 12Z is shaded for clarity. The position of the cross-section of Figures 5 and 6 is also shown. . . . . .

5 Vertical cross-section through the fold along 6W showing θ_w (thick contours) and PV (thin contours, the dashed line indicates the 2PVU surface) at 12Z. The shaded region indicates where the relative humidity is below 30%. The contour intervals are 2K and 1PVU. . . . . .

6 As for Figure 5 but with data from the LAM (50km horizontal resolution, 19 levels in the vertical). . . . . .

7 Vertical cross-section at about 8W of unmodifed PV at 6Z. Contour interval 0.5PVU; the thick contour corresponds to the 2PVU surface. The dashed dashed contours show potential temperature, contour interval is 4K. The PV anomalies F and S are explained in the text. . . . . .

8 Same cross-section as Figure 7 with the tropopause fold (A) removed. Contour interval 0.5PVU, the thick contour corresponds to the 2PVU surface. The dashed contours show the potential temperature associated with the PV of the "flat" tropopause; contour interval is 4K . . . . . .

9 PV anomaly associated with the fold (F). (a) Vertical cross-section at about 8W of the PV anomaly at 6Z, (b) horizontal cross-section at 400mb of the PV anomaly at 6Z. The 'L' marks the centre of the surface low at this time. The dashed line in (b) shows the position of the cross-sections of Figures 7, 8, 9a and 10. Contour interval 0.5PVU; the thick contour corresponds to the 2PVU surface . . . . . .

10 Vertical cross-section at 8W at 6Z showing the stratospheric anomaly (S). Contour interval 0.5PVU; the thick contour corresponds to the 2PVU surface

11 Fields attributable to the full PV field at 6Z; (a) the vectors show the difference between the wind at 900mb and 700mb, the contours are θ_w at 800mb, contour interval 1K. The scale arrow in the bottom left-hand corner represents a wind difference of 5 ms^{-1}. In (b) we show θ_w (solid) and θ (dashed) at 800mb with a contour interval of 1K. In this and subsequent figures the shaded area depicts the position of the PV anomaly corresponding to PV=1.5 at 500mb, the coastline is dotted. . . . . .

12 Contour plots to show the generation of instability at 6Z due to (a) the full PV field and (b) the 'flat' tropopause case. The thick solid line shows where $\frac{\partial \theta_w}{\partial z} = 0$. The thin contours show (a) the destabilisation due to the winds associated with the full tropopause $\left(\frac{\partial \mathbf{u}}{\partial z}.\nabla_h \theta_w\right)$, (b) the destabilisation due to the winds associated with the flat tropopause $\left(\frac{\partial \overline{\mathbf{u}}}{\partial z}.\nabla \theta_w\right)$. Negative values are depicted by dashed contours and positive by solid contours. The contour interval is $1 \times 10^{-8} K m^{-1} s^{-1}$. . . . . .

13 Contour plot showing $\frac{d\theta_w}{dz}$ over the layer 900mb - 700mb at 6Z. The contour interval is $1 \times 10^{-4} K m^{-1}$, the bold line shows the zero contour. . . . . .

14 Vertical profile of maximum$|\nabla_h \theta|$ at 6Z in the region shown in Figure 12 for the case with no alteration of the PV (solid curve) and for the case where the PV fold has been removed (dashed line). See text for more detail. . .

15 Difference between the winds at 900mb and 700mb attributable to the PV fold at 6Z, the thin contours show θ_w at 800mb, contour interval 1K. The bold contour shows where $\frac{\partial \theta_w}{\partial z} = 0$. The scale arrow in the bottom left-hand corner represents a wind difference of 5 ms^{-1}. . . . . .

16 Contour plot to show the size of the second term on the right hand side of equation (4) at 6Z. Physically, this term can be described as the rate of destabilisation due to the winds associated with the tropopause fold $\left(\frac{\partial \mathbf{u}'}{\partial z}.\nabla \theta_w\right)$. The coastline is dotted, the shaded area shows the area of the PV fold (PV=1.5PVU at 500mb). The bold contour shows where $\frac{\partial \theta_w}{\partial z} = 0$. Negative values are depicted by dashed contours and positive by solid contours. The contour interval is $1 \times 10^{-8} K m^{-1} s^{-1}$. . . . . .

17 Plots showing the two trajectories. In each case the solid lines represents trajectory A and the dashed line represents trajectory B. (a) Horizontal projection of the average trajectories, as defined in the text, starting at 6Z and ending at 18Z. (b) Plot showing the variation of $\frac{d\theta_w}{dz}$ along the trajectories, and (c) Plot showing the variation of pressure along the trajectories.

	Rate of generation of potential instability due to:			
	flat tropopause $\left(\frac{\partial \overline{\mathbf{u}}}{\partial z}.\nabla_h \theta_w\right)$	tropopause fold $\left(\frac{\partial \mathbf{u}'}{\partial z}.\nabla \theta_w\right)$	total field $\left(\frac{\partial \mathbf{u}}{\partial z}.\nabla \theta_w\right)$	% due to PV anomaly
5.1W,50.2N (fold F)	1.3	3.1	4.3	70
4.6W,50.5N (fold F)	5.4	2.5	7.9	31
3.2W,49.9N (fold F)	-2.7	2.9	0.3	
5.8W,50.4N (strat anom S)	5.3	.25	4.8	5
6.0W,50.6N (fold F, Neumann)	3.1	1.6	4.8	34

Table 1: Table showing the size of each term on the right-hand side of equation (4) ($K(km)^{-1}(day)^{-1}$) calculated at the points indicated in the the first column and at 6Z. The second column shows the rate of generation of potential instability due the the "flat" tropopause, the third column shows the rate of generation of potential instability due to the anomaly alone, the fourth column shows the total rate of generation of potential instability and the final column shows the percentage associated with the anomaly (note no percentage is given where the contributions are of opposite signs). The first three rows relate to the effect of the tropopause fold and the Dirichlet boundary condition. The fourth row relates to values where the effect of the stratospheric anomaly is a maximum. The final row corresponds to the position where the generation of instability due to the fold is maximum but with the Neumann condition in place of the Dirichlet condition used in the other rows.

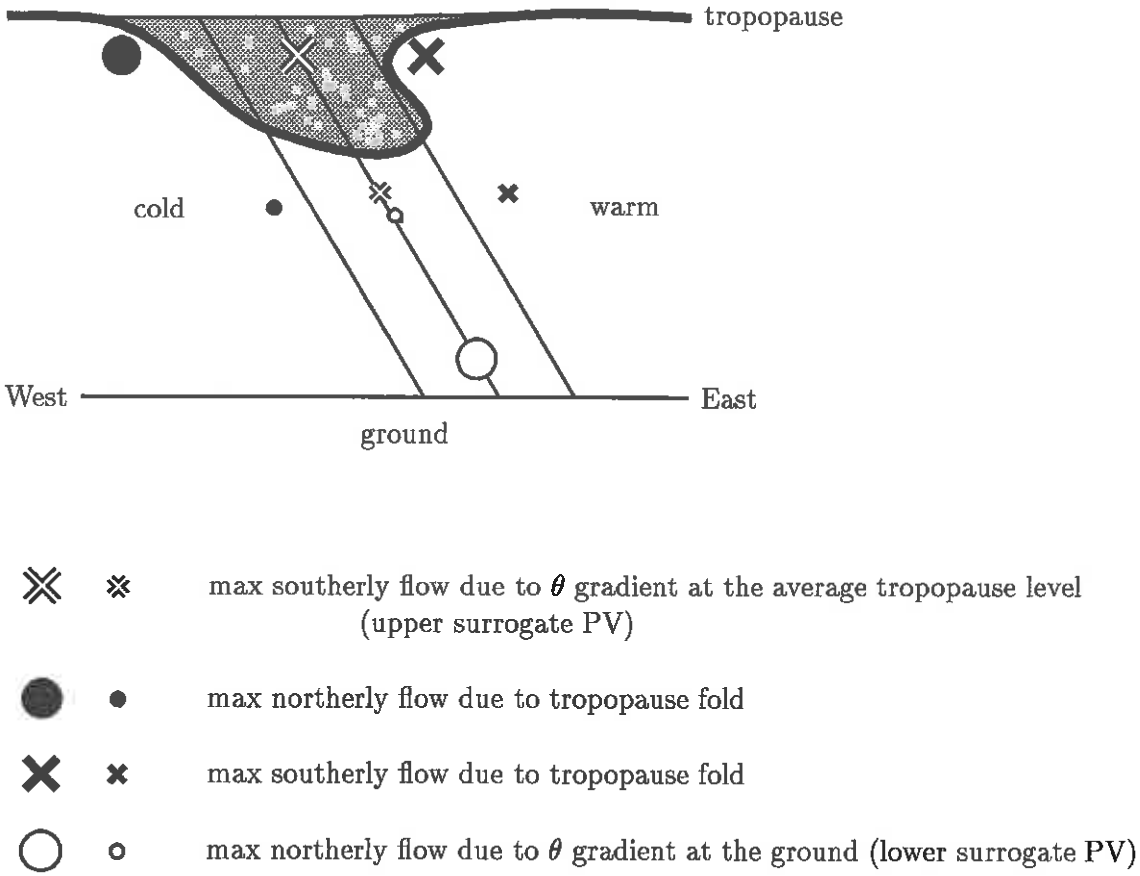

Figure 1: Schematic diagram of a tropopause fold (thick line) and frontal zone (thin lines) showing the contribution to the wind in the troposphere associated with three features - the PV fold (indicated by shading), the temperature gradient on the upper boundary (indicated by the upper thin horizontal line) and the temperature gradient on the lower boundary. The strength of the flow is proportional to the size of the symbols.

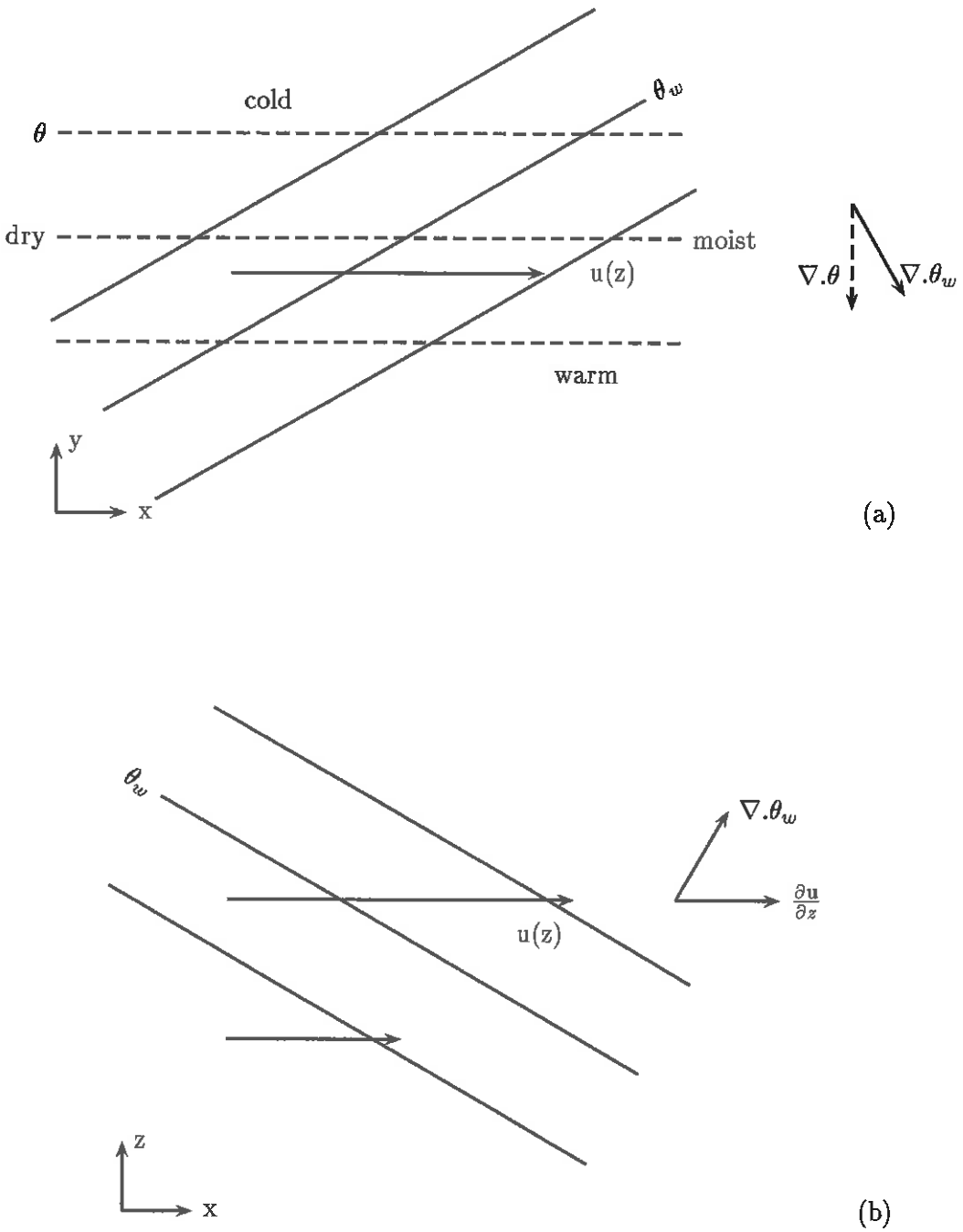

Figure 2: Diagram showing configuration of θ and θ_w with associated wind and moisture fields which gives rise to the generation of potential instability. In (a) a horizontal section is shown, the solid lines denote contours of θ_w, the dashed lines show θ, the vector denotes the direction of the thermal wind. In (b) a vertical section is shown; again the solid lines indicate θ_w and the vectors show the thermal wind. Vector representations of the terms on the right-hand sides of equations (3) and (2) are shown on the right hand sides of diagrams (a) and (b) respectively.

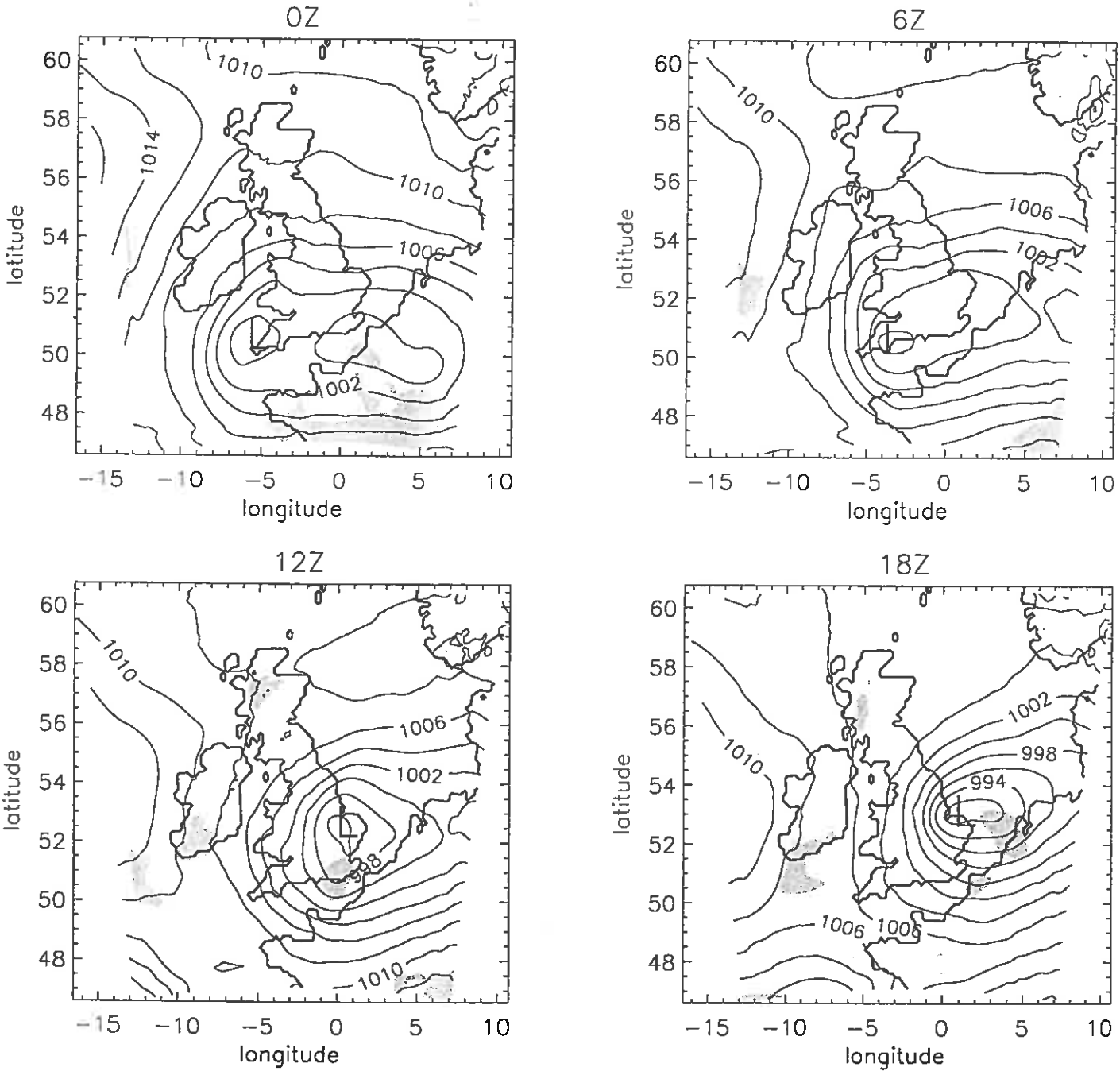
0Z
6Z
12Z
18Z
latitude
longitude
60
58
56
54
52
50
48
−15
−10
−5
0
5
10
1010
1014
1006
1002
998
994

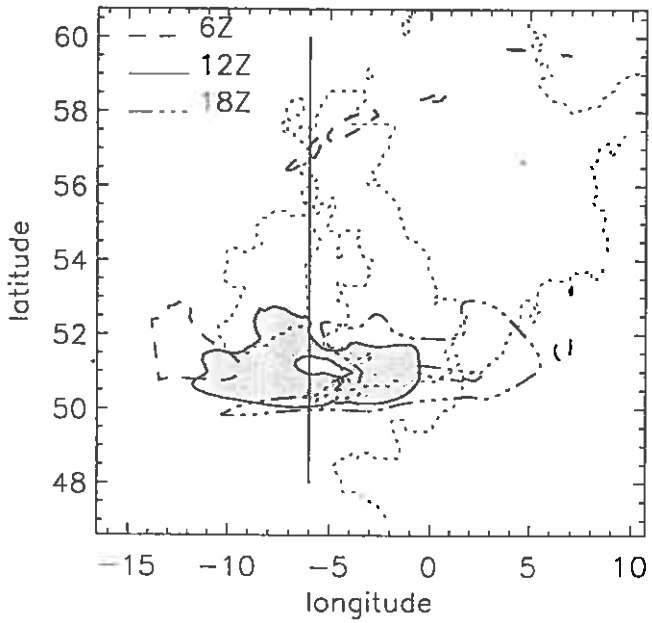
6Z
12Z
18Z
60
58
56
54
52
50
48
latitude
−15
−10
−5
0
5
10
longitude

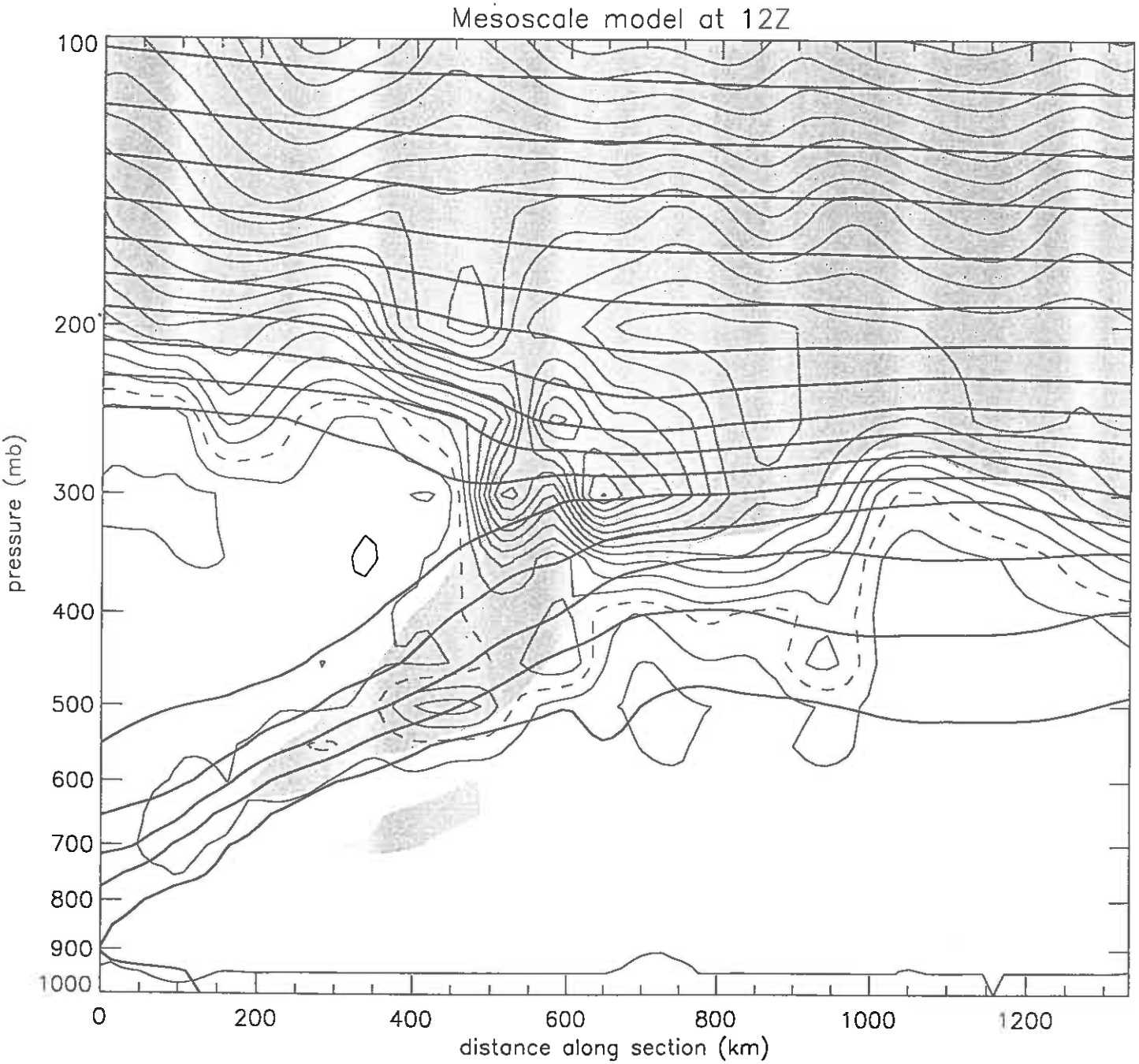
Mesoscale model at 12Z
pressure (mb)
100
200
300
400
500
600
700
800
900
1000
0
200
400
600
800
1000
1200
distance along section (km)

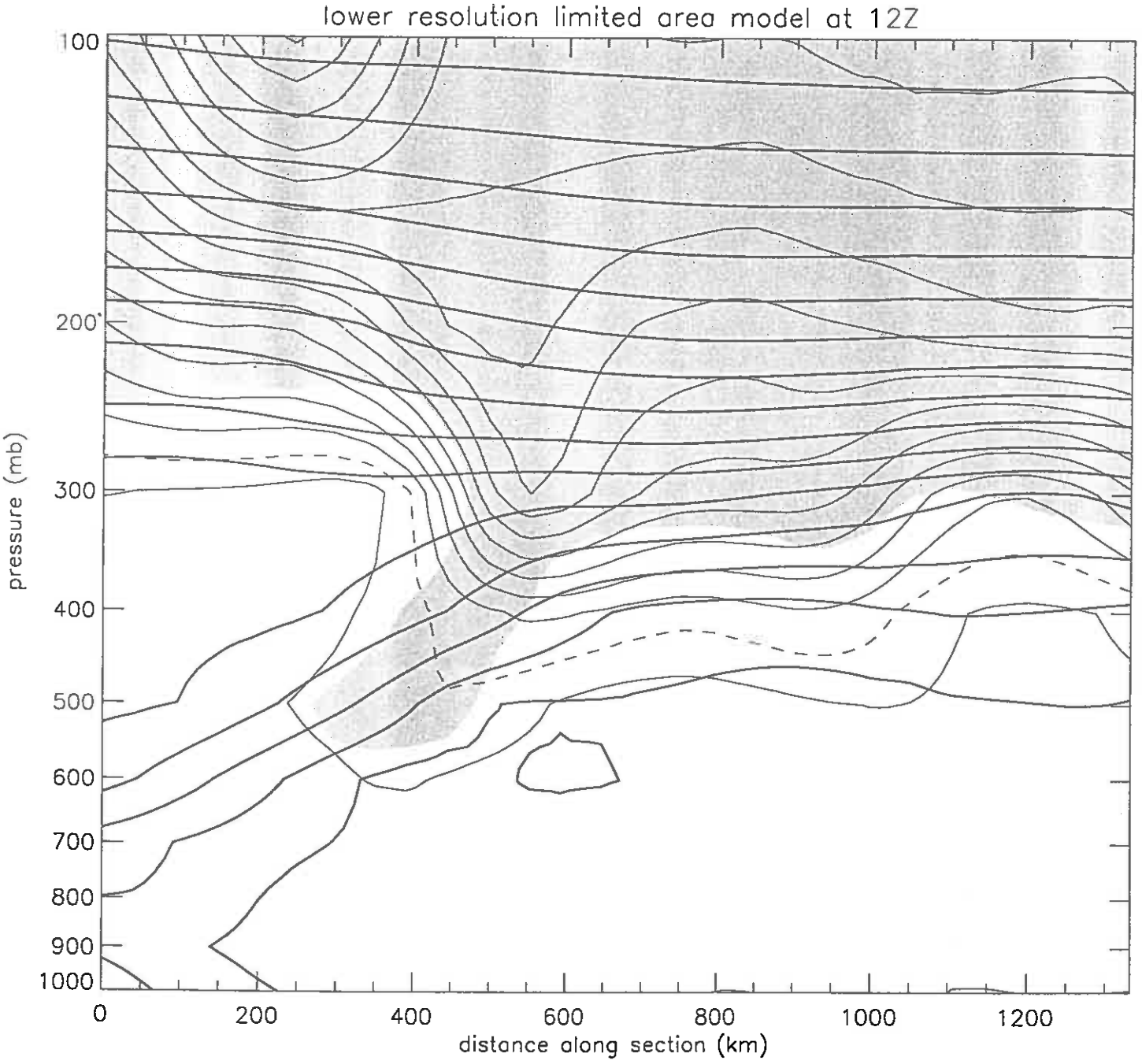
lower resolution limited area model at 12Z
pressure (mb)
100
200
300
400
500
600
700
800
900
1000
0
200
400
600
800
1000
1200
distance along section (km)

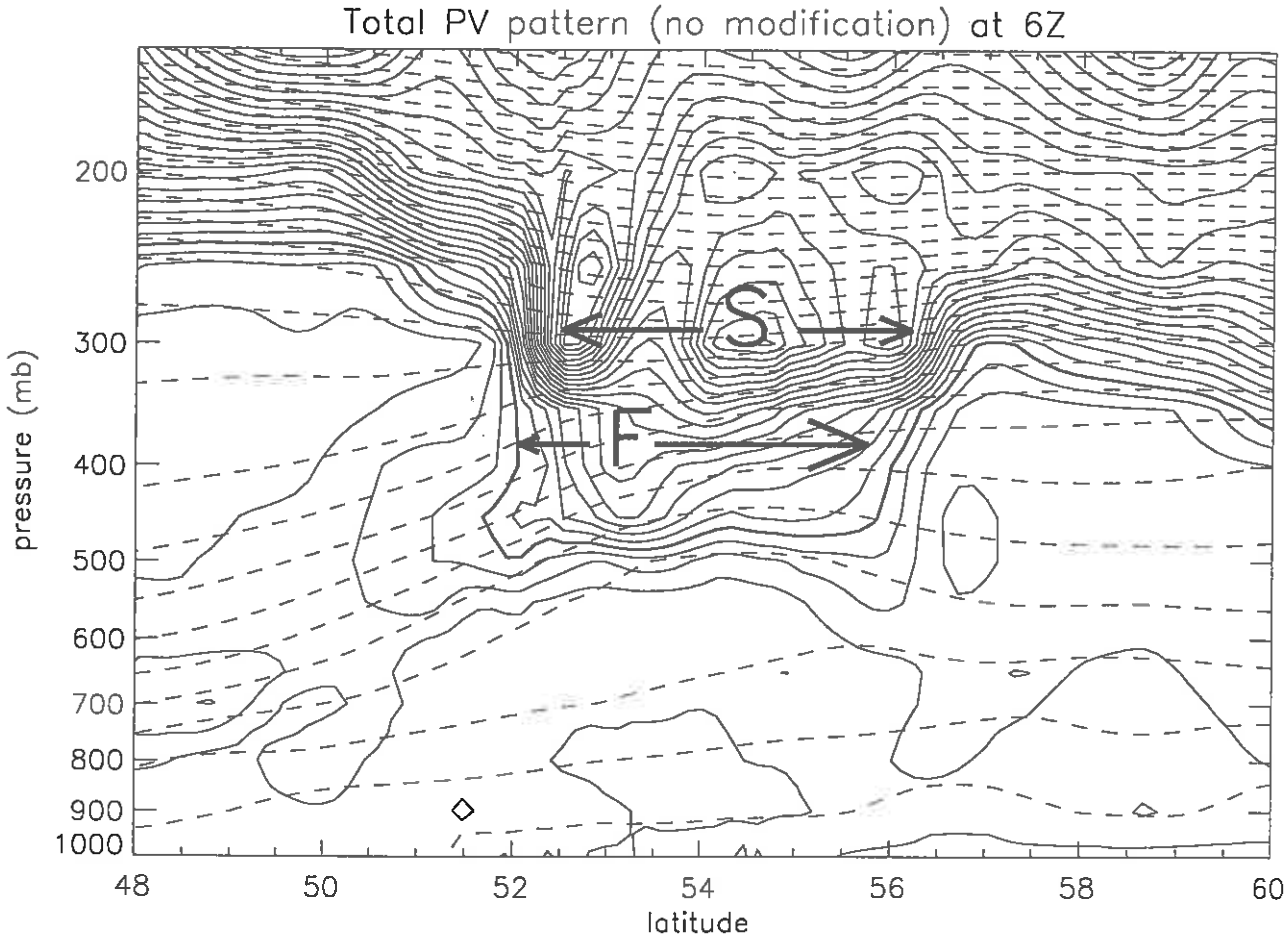
Total PV pattern (no modification) at 6Z
pressure (mb)
200
300
400
500
600
700
800
900
1000
S
F
48
50
52
54
56
58
60
latitude

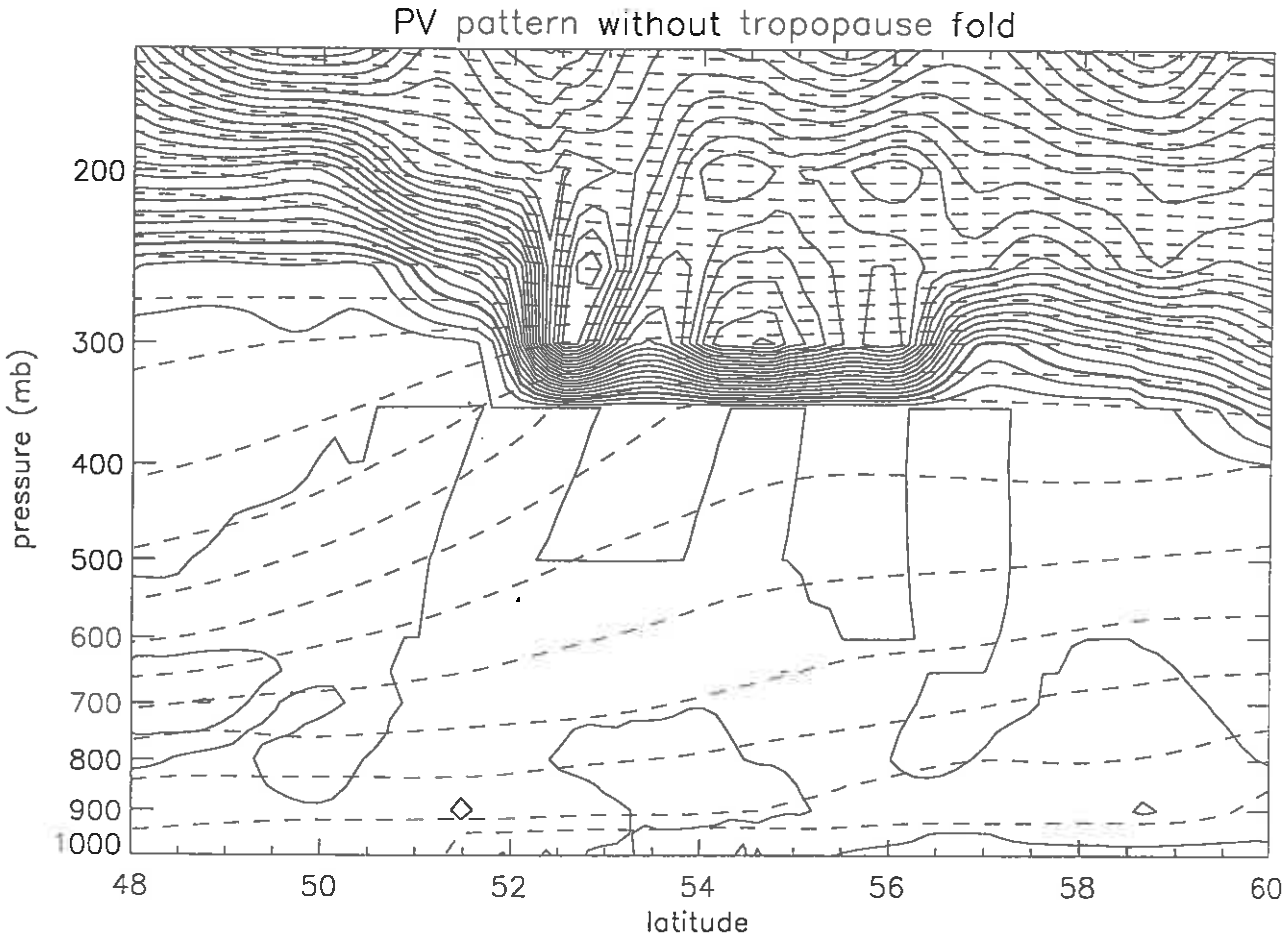
PV pattern without tropopause fold
pressure (mb)
200
300
400
500
600
700
800
900
1000
48
50
52
54
56
58
60
latitude

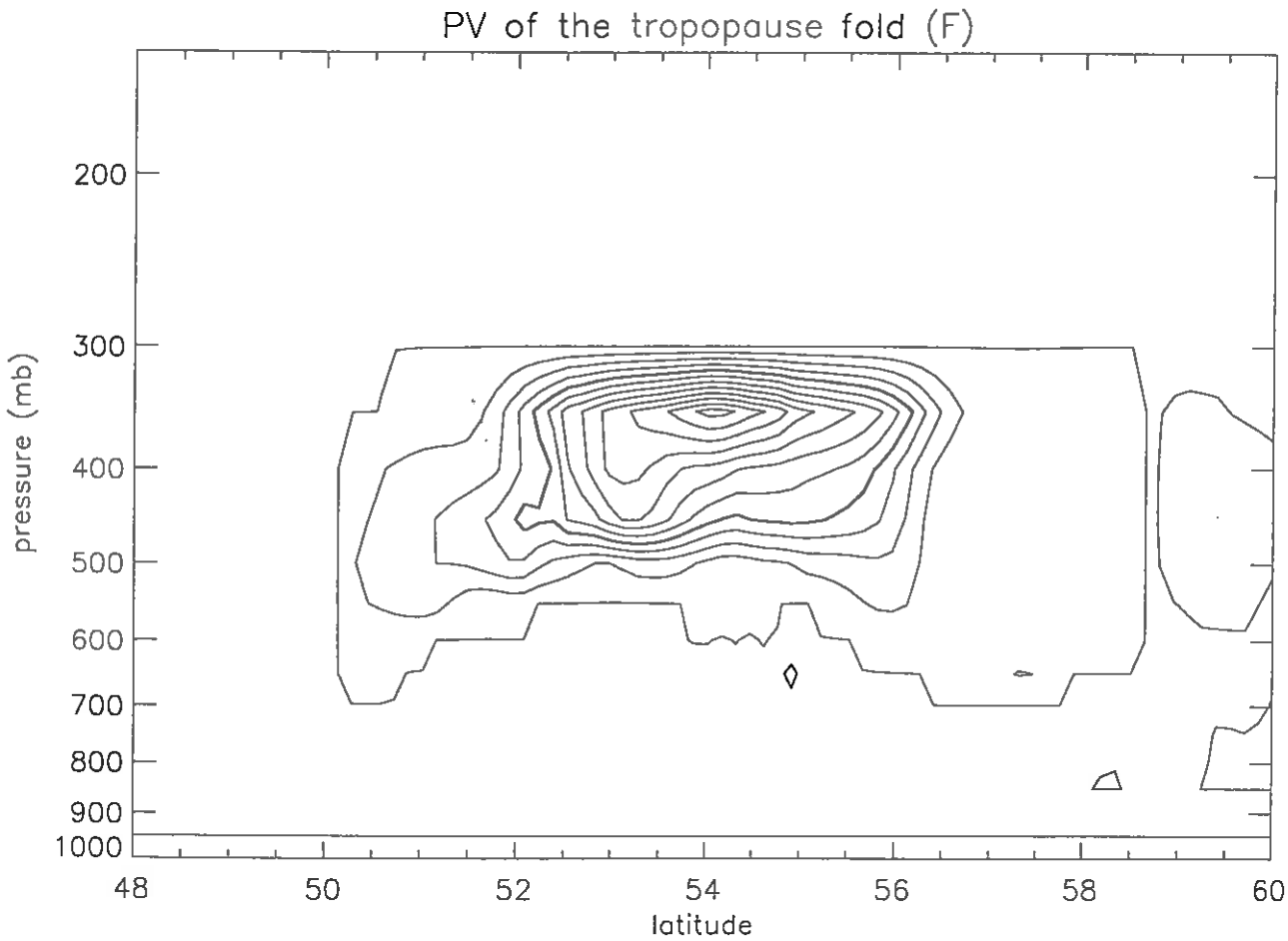
PV of the tropopause fold (F)
pressure (mb)
200
300
400
500
600
700
800
900
1000
48
50
52
54
56
58
60
latitude

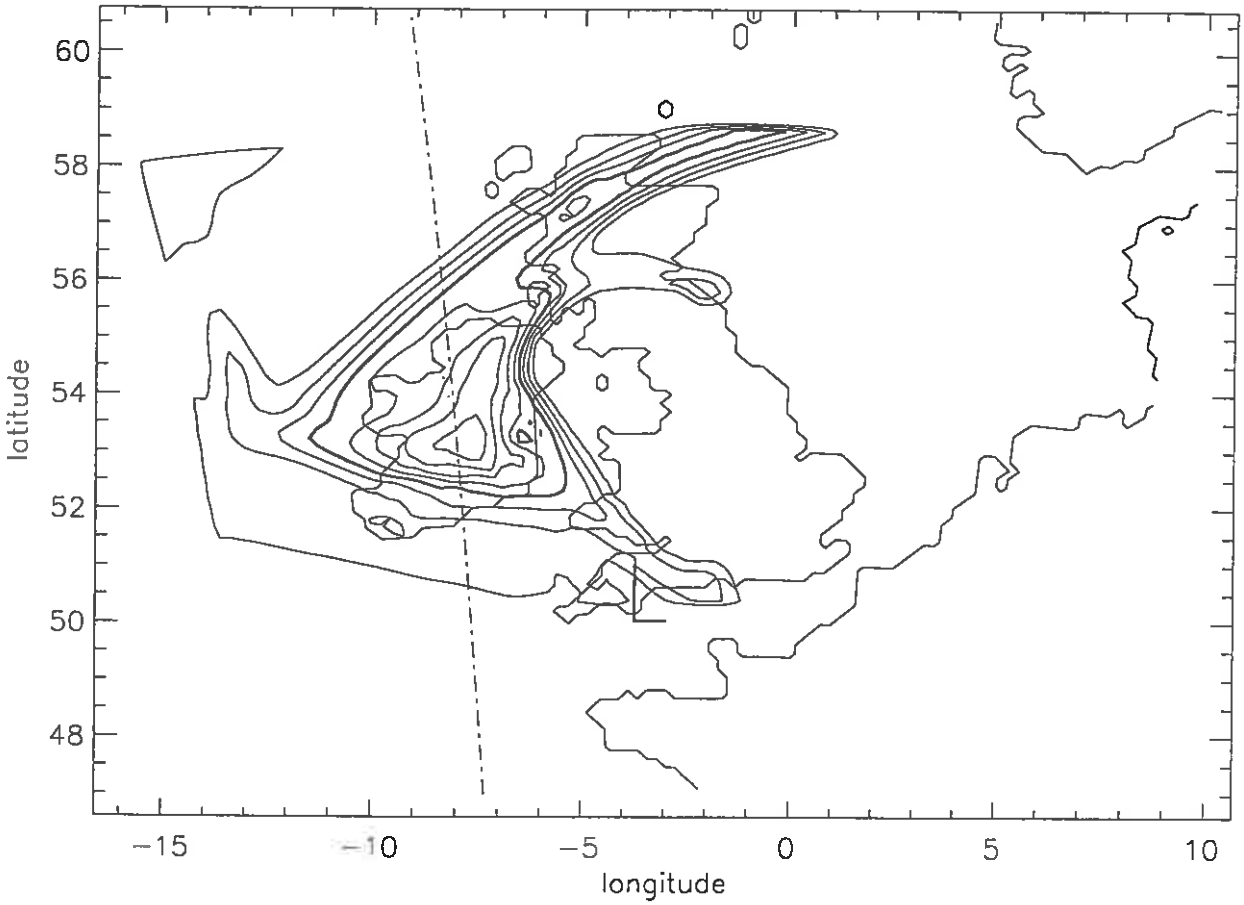
60
58
56
54
52
50
48
latitude
−15
−10
−5
0
5
10
longitude

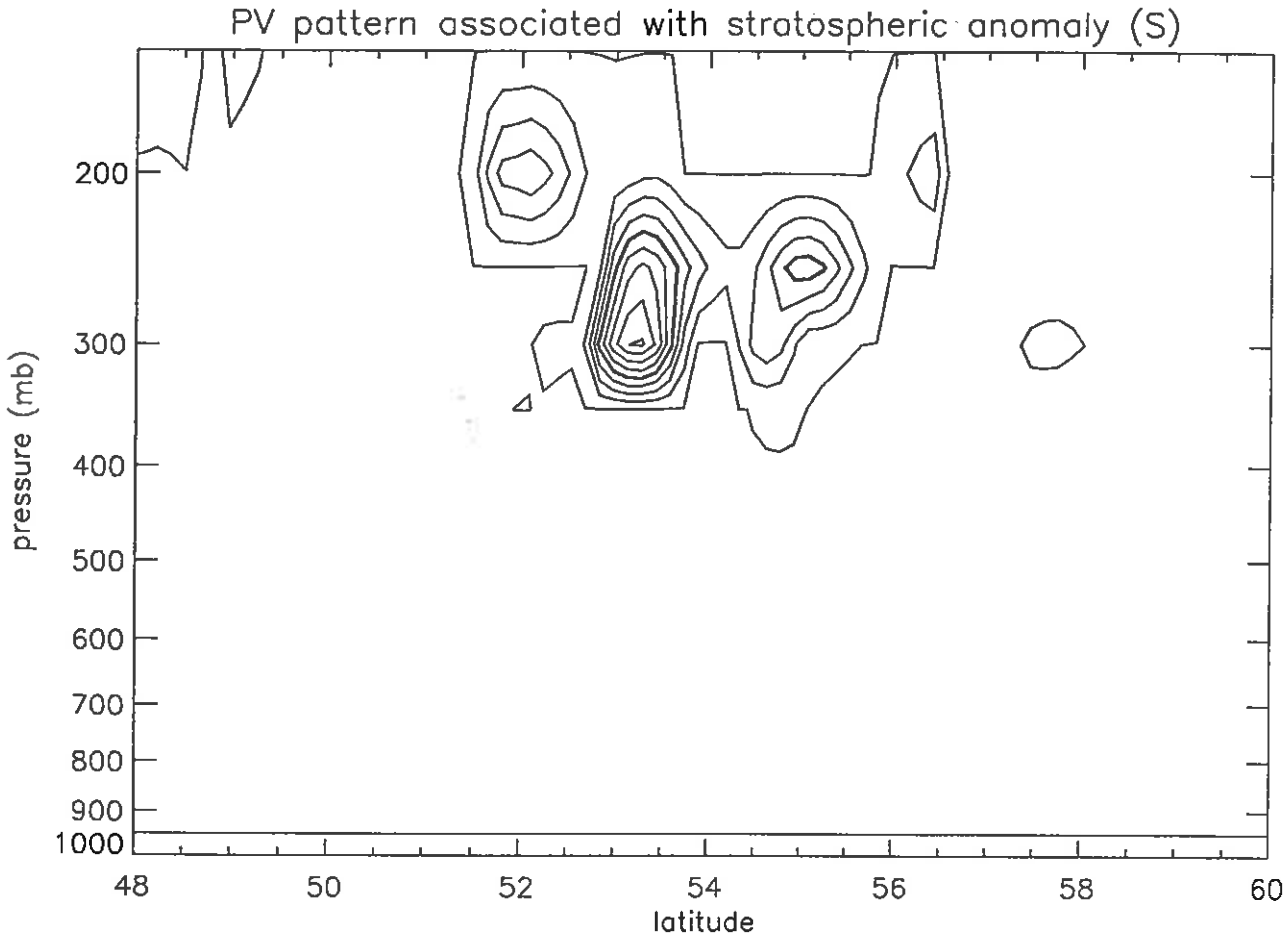
PV pattern associated with stratospheric anomaly (S)
pressure (mb)
200
300
400
500
600
700
800
900
1000
48
50
52
54
56
58
60
latitude

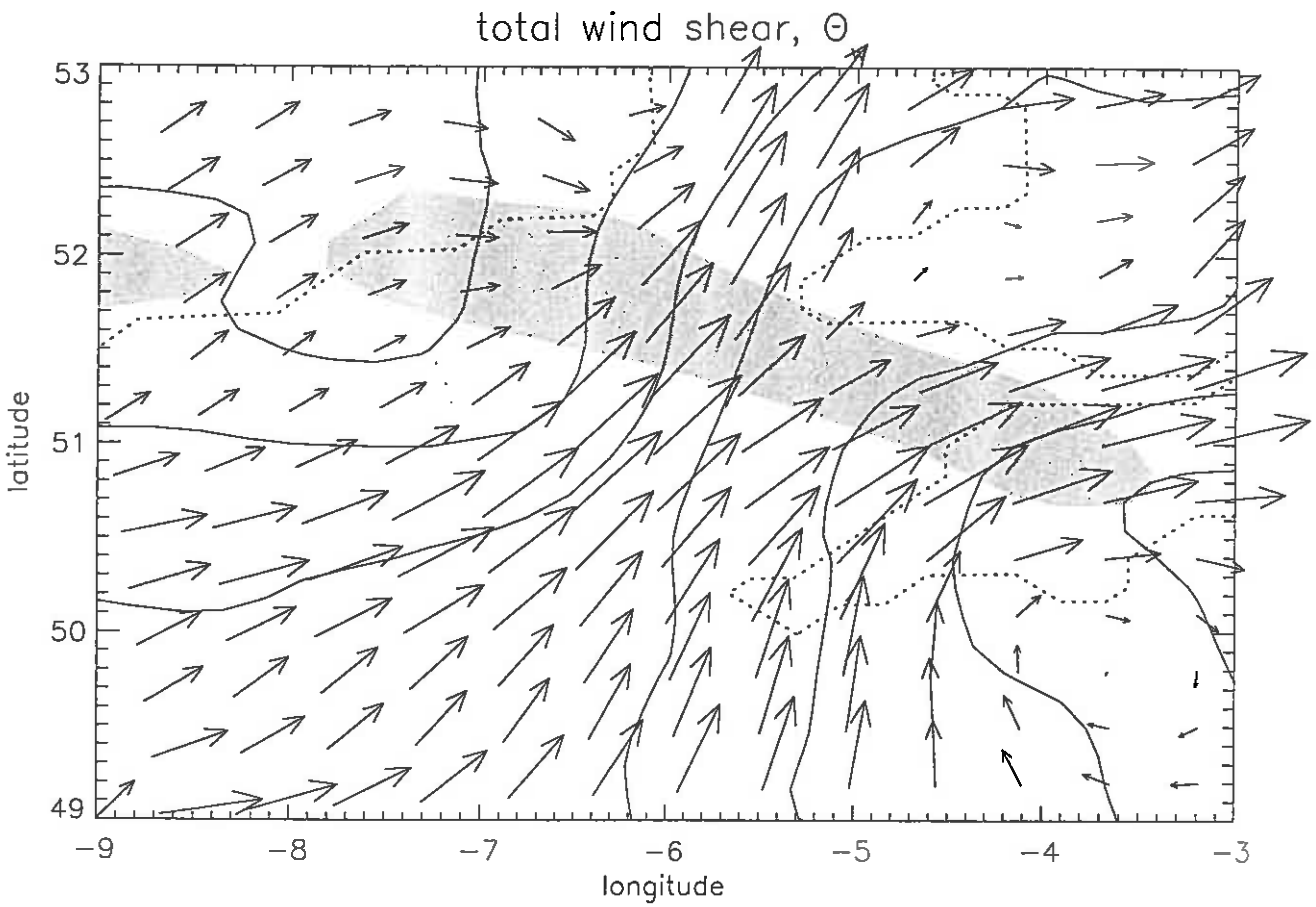
total wind shear, Θ
53
52
51
50
49
latitude
−9
−8
−7
−6
−5
−4
−3
longitude

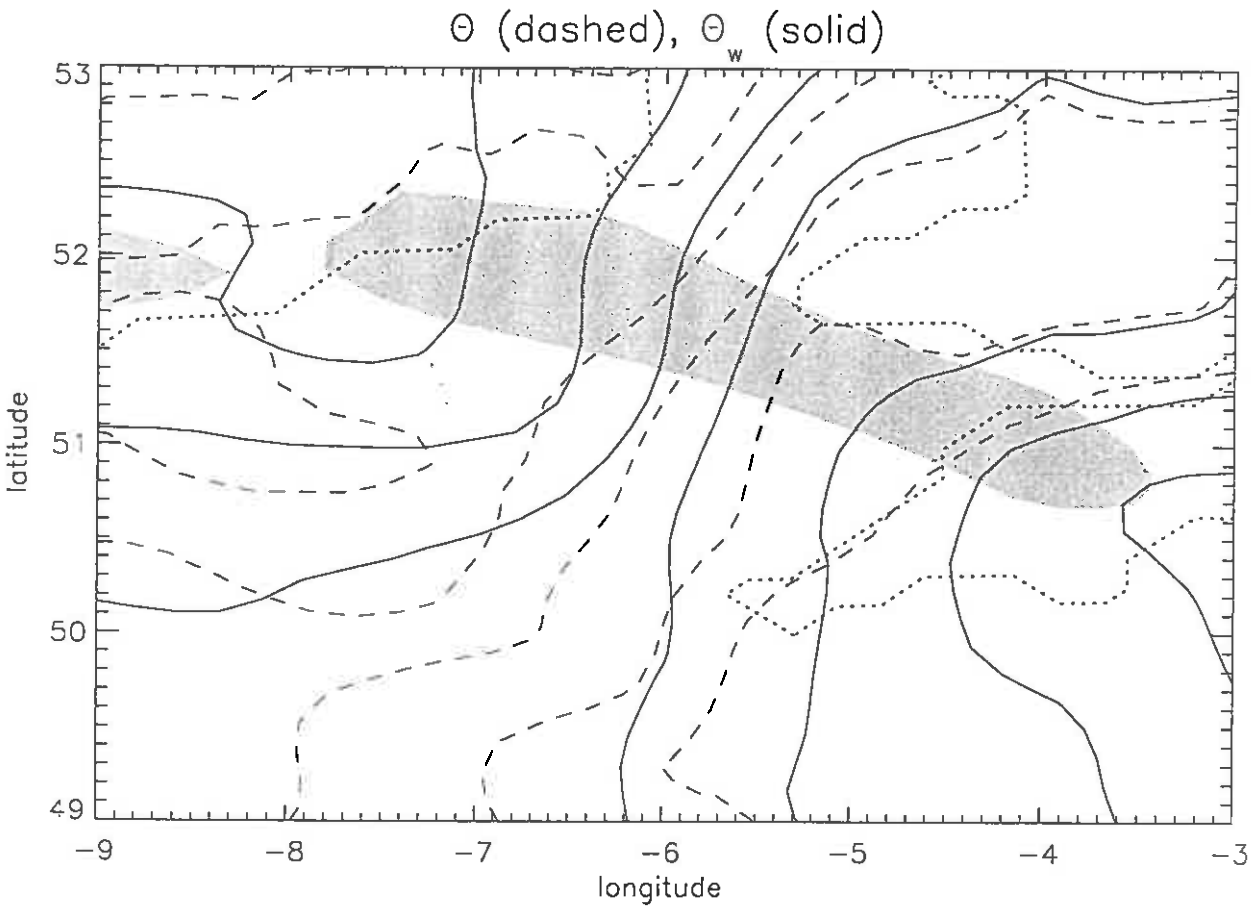
Θ (dashed), Θw (solid)
53
52
51
50
49
latitude
−9
−8
−7
−6
−5
−4
−3
longitude

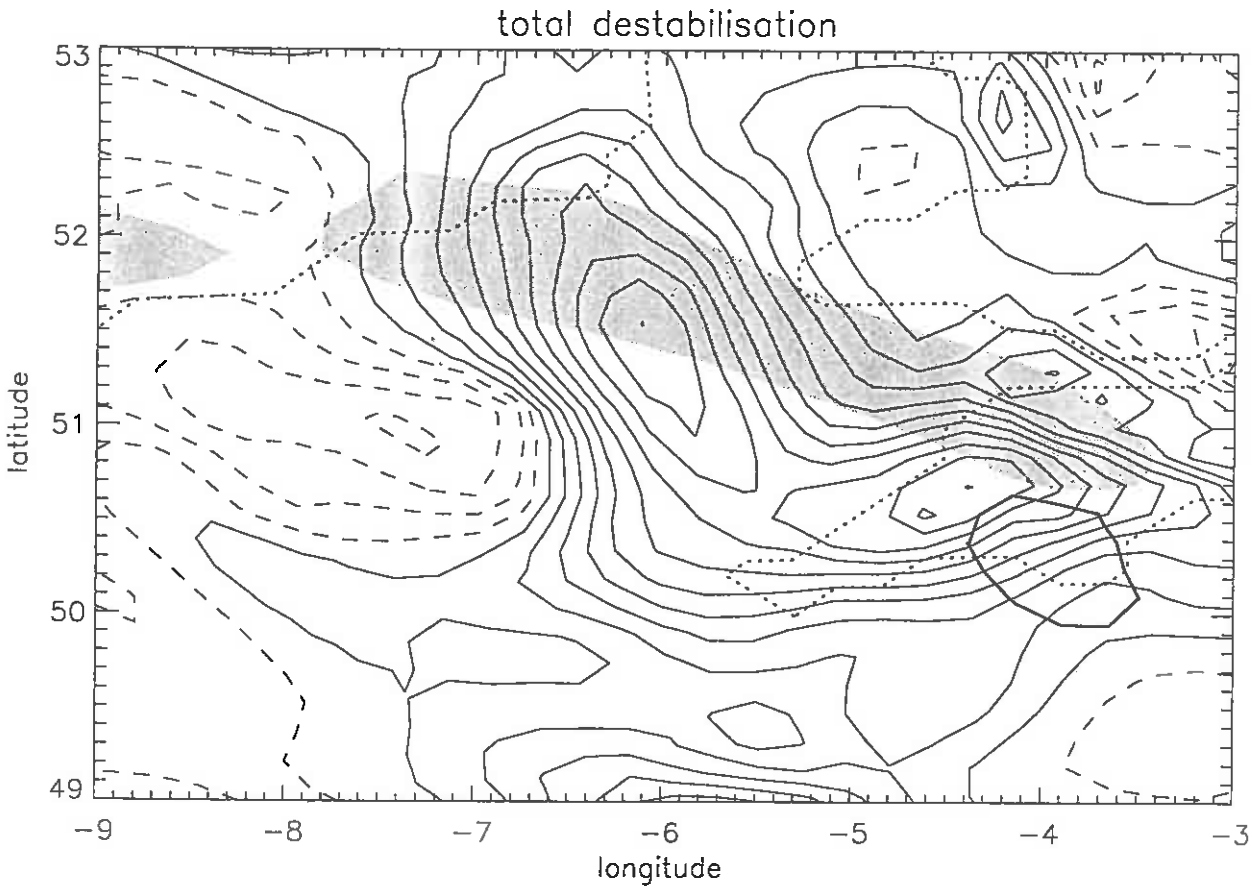
total destabilisation
53
52
51
50
49
latitude
−9
−8
−7
−6
−5
−4
−3
longitude

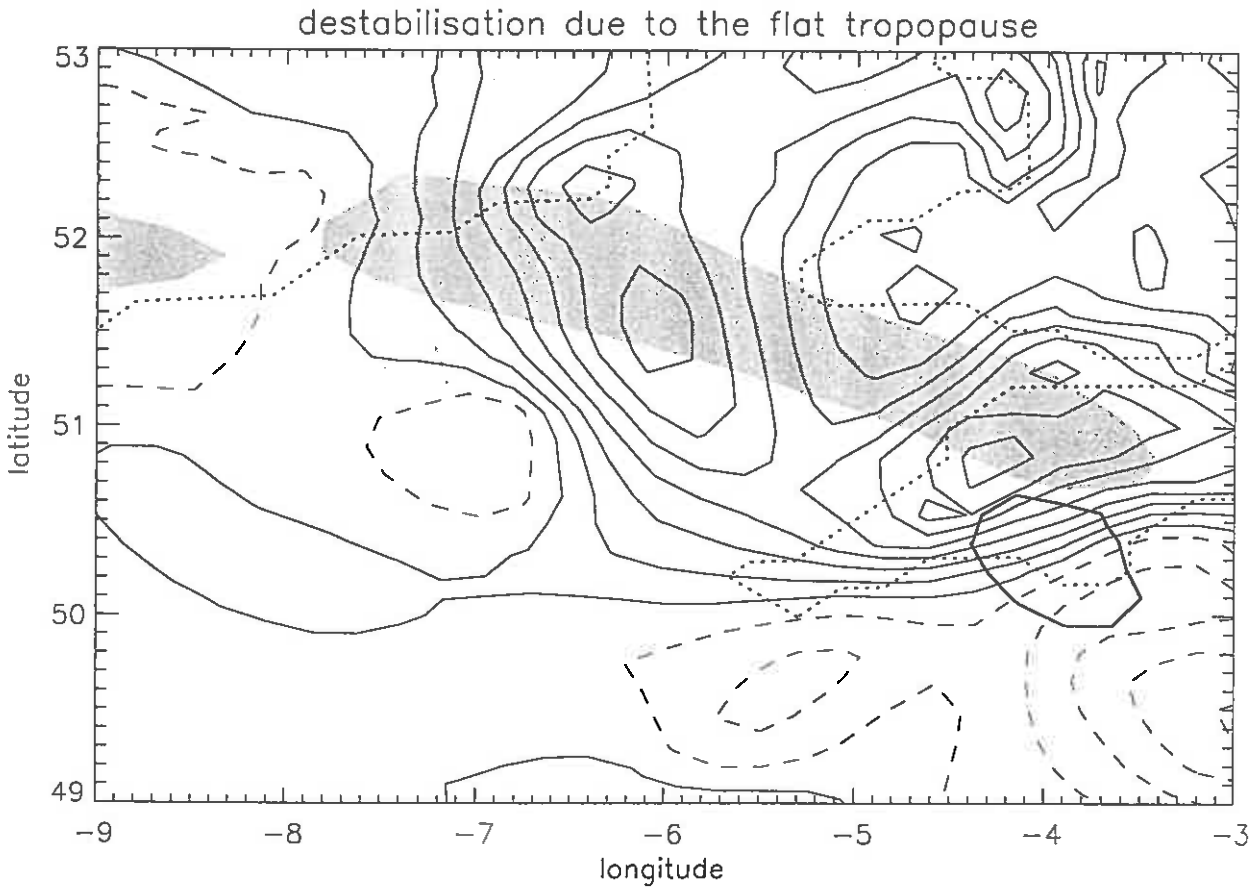
destabilisation due to the flat tropopause
53
52
51
50
49
latitude
−9
−8
−7
−6
−5
−4
−3
longitude

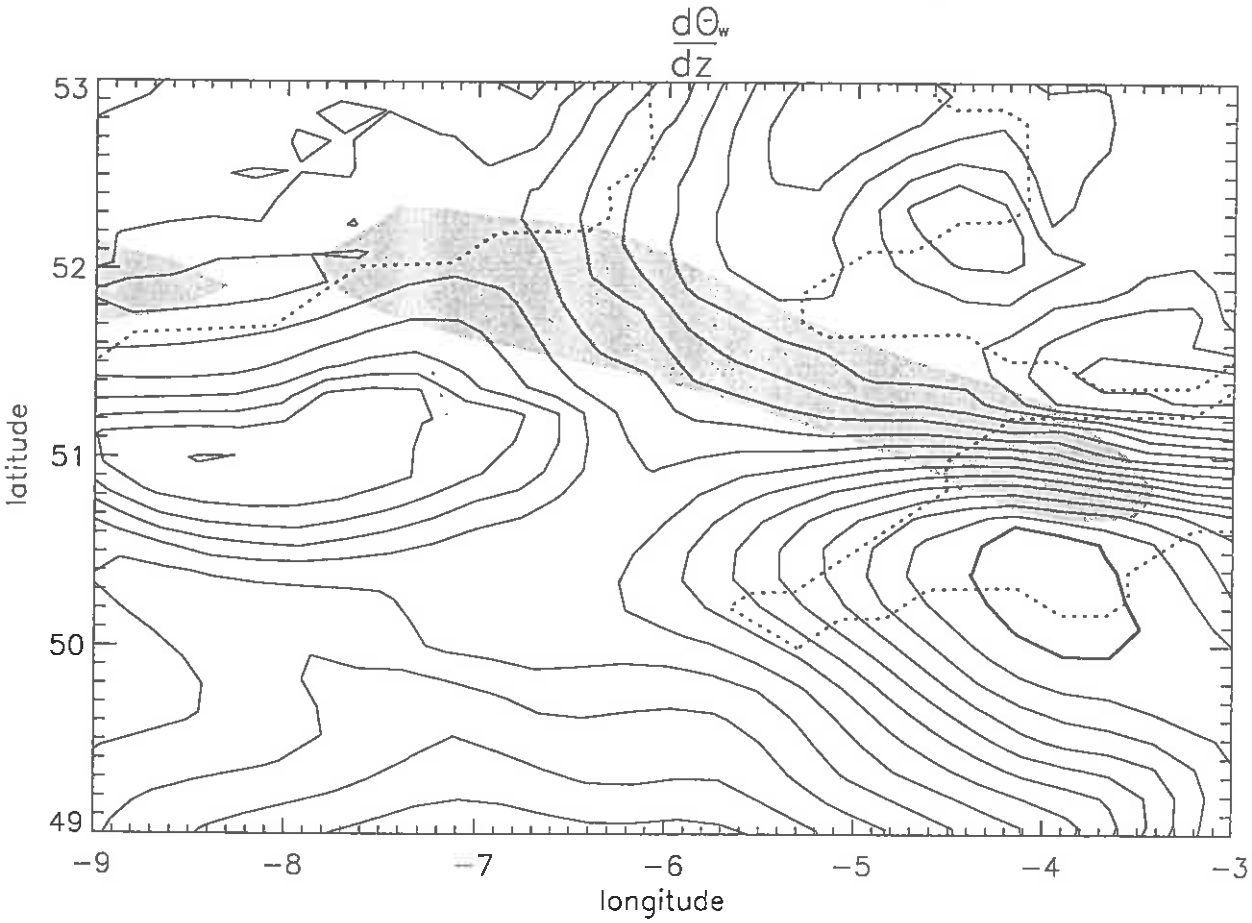
dΘw/dz
53
52
51
50
49
latitude
−9
−8
−7
−6
−5
−4
−3
longitude

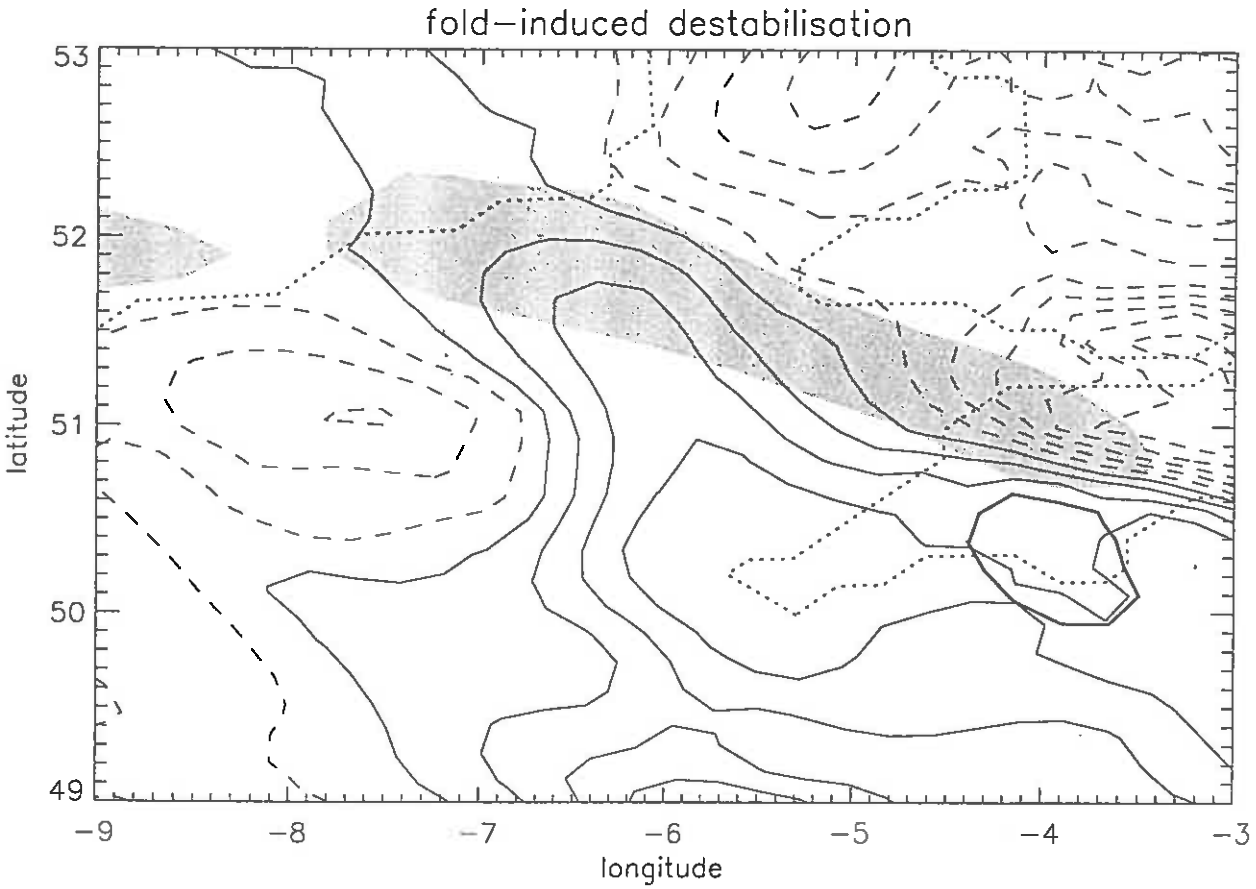
fold–induced destabilisation
53
52
51
50
49
latitude
−9
−8
−7
−6
−5
−4
−3
longitude

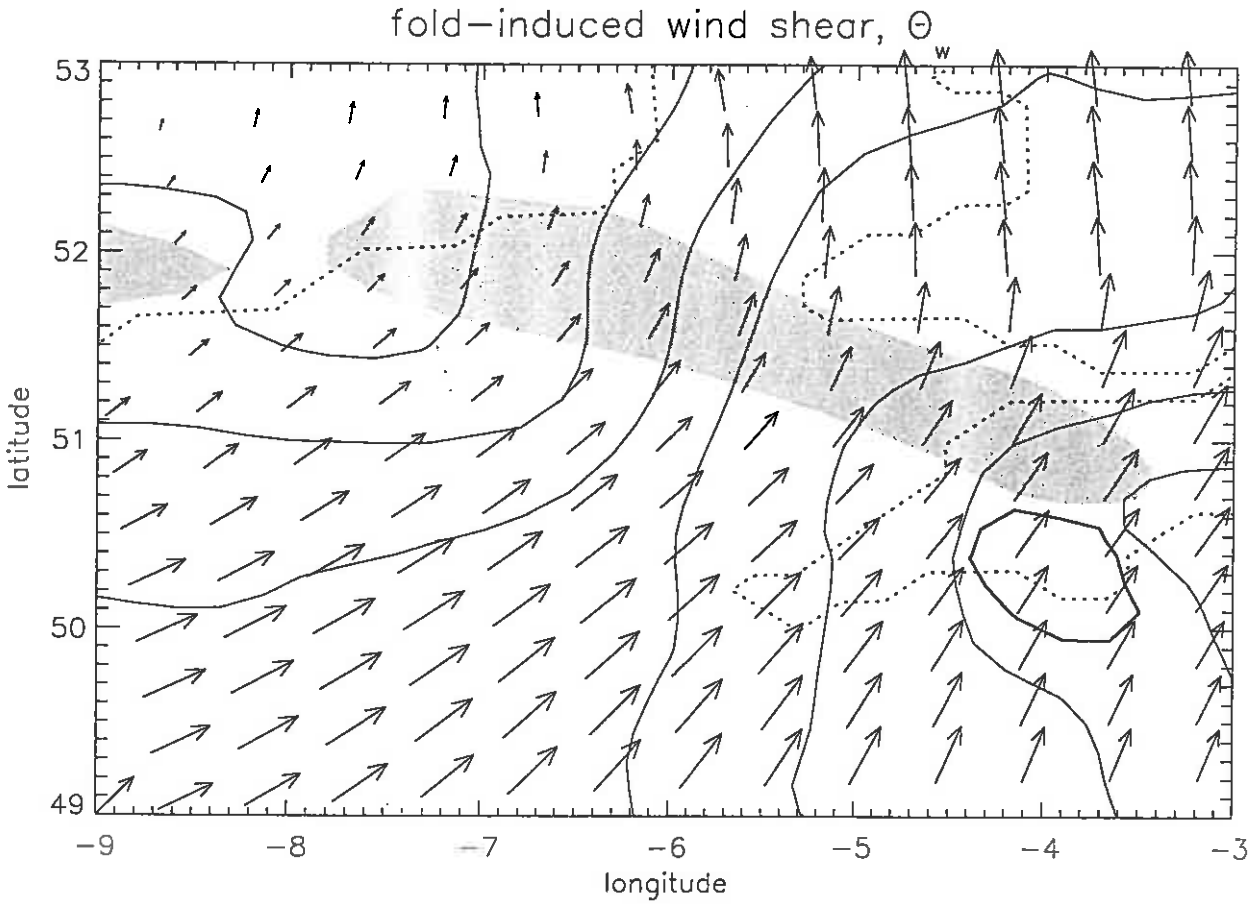
fold–induced wind shear, Θ
W
53
52
51
50
49
latitude
−9
−8
−7
−6
−5
−4
−3
longitude

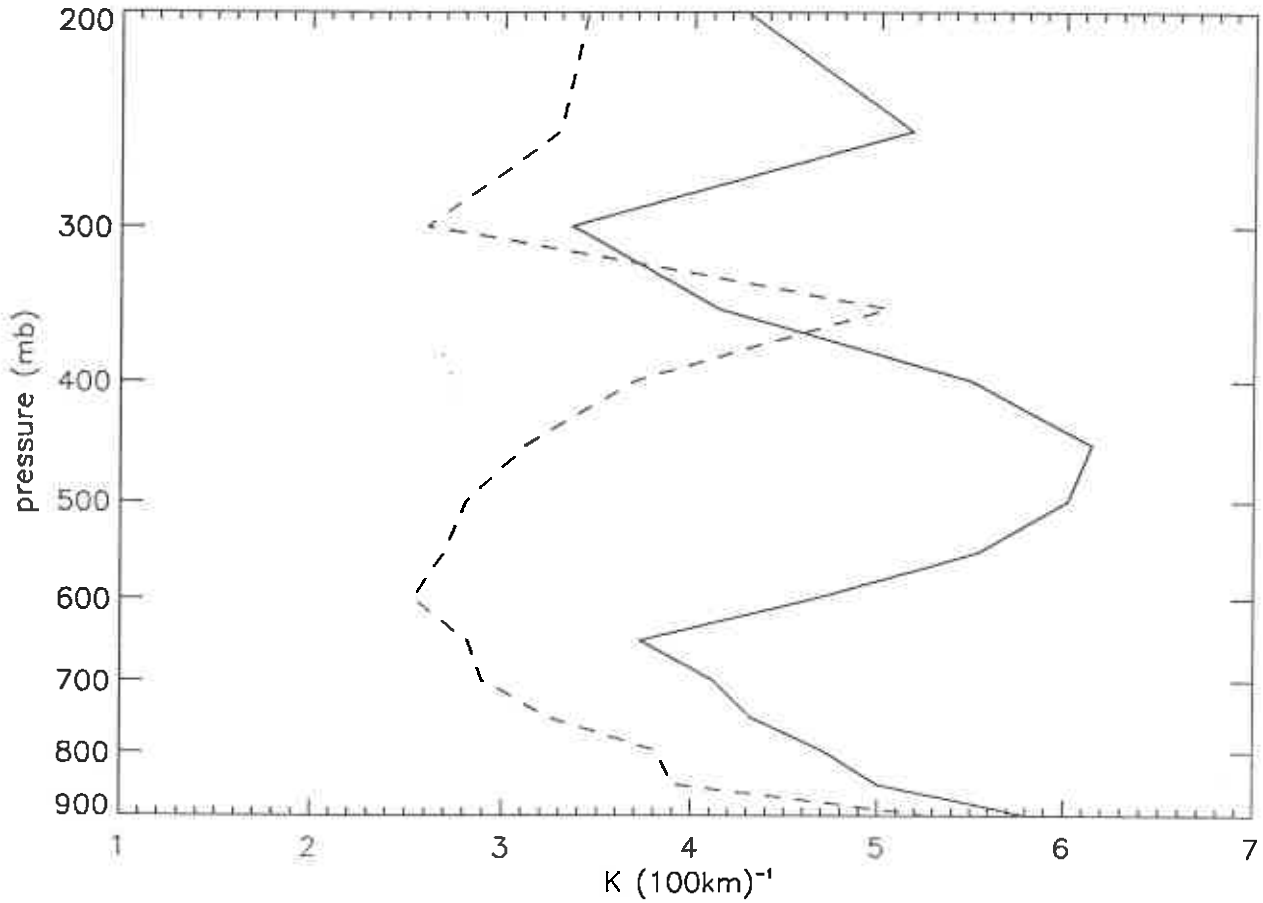
200
300
400
500
600
700
800
900
pressure (mb)
1
2
3
4
5
6
7
K (100km)⁻¹

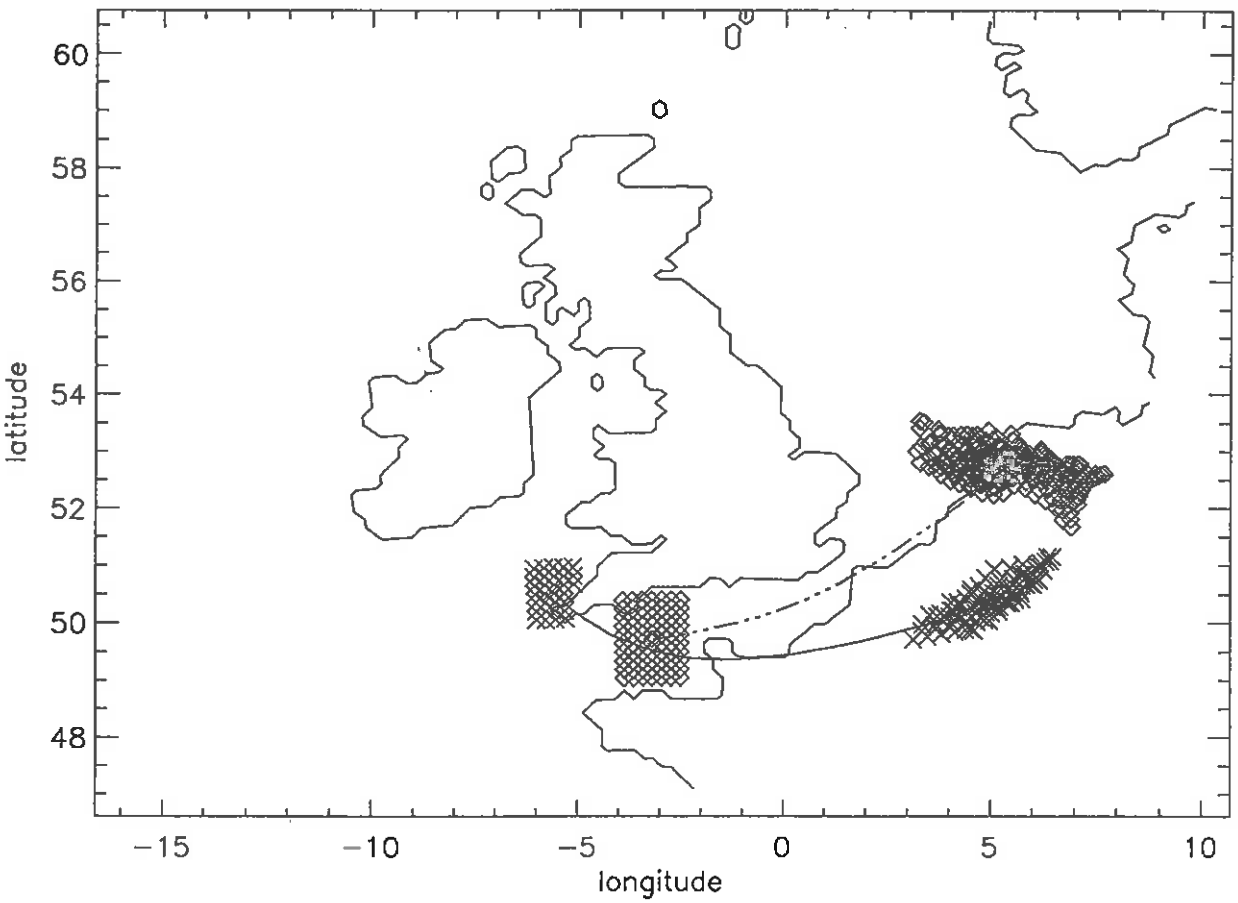
60
58
56
54
52
50
48
latitude
−15
−10
−5
0
5
10
longitude

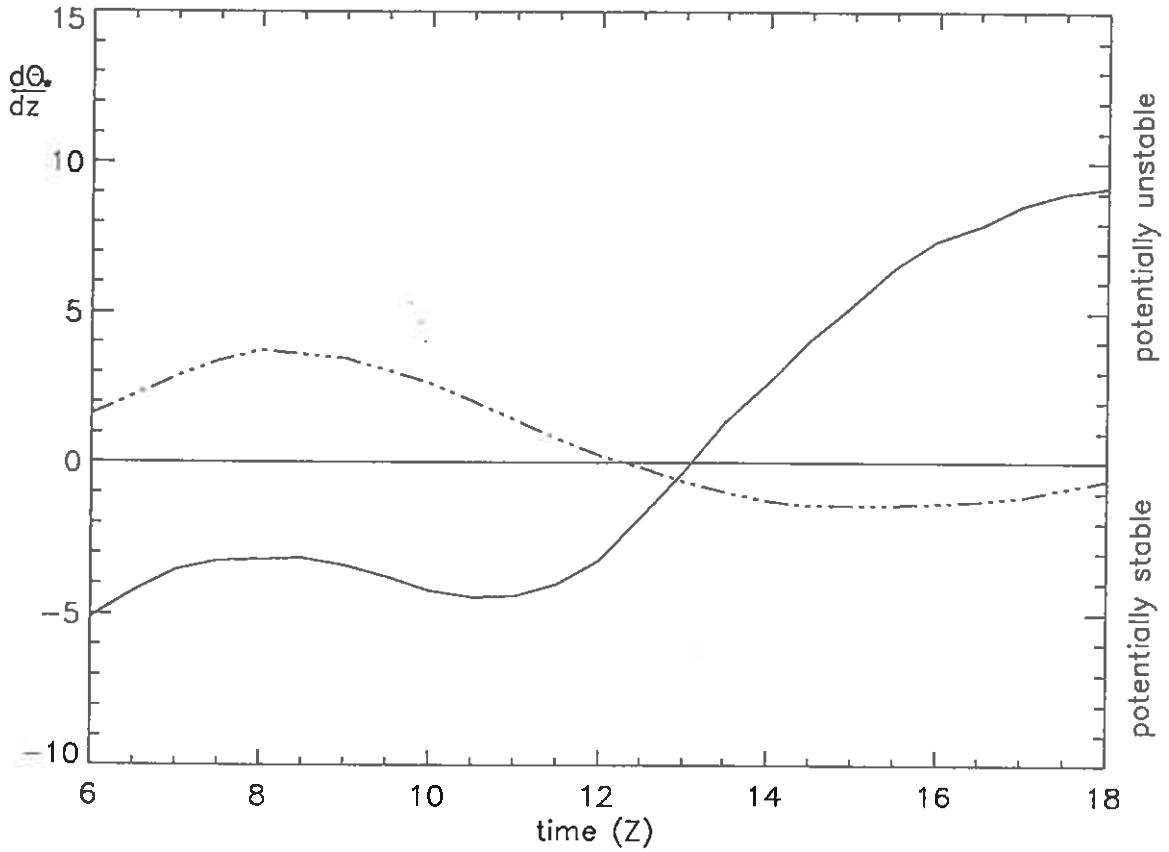
15
10
5
0
−5
−10
$\frac{d\Theta_e}{dz}$
6
8
10
12
14
16
18
time (Z)
potentially unstable
potentially stable

17c

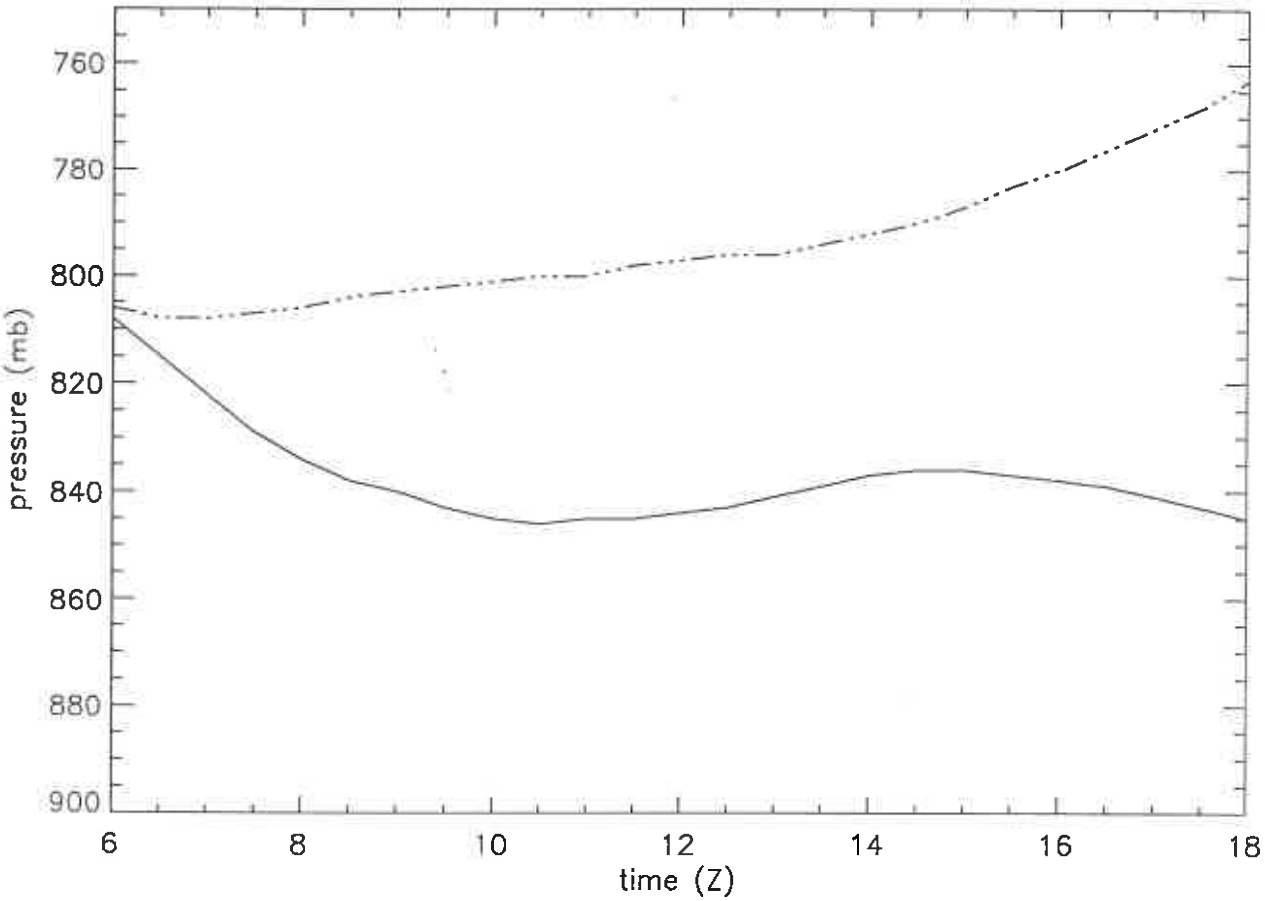
760
780
800
820
840
860
880
900
pressure (mb)
6
8
10
12
14
16
18
time (Z)

CURRENT JCMM INTERNAL REPORTS

This series of JCMM Internal Reports, initiated in 1993, contains unpublished reports and also versions of articles submitted for publication. The complete set of Internal Reports is available from the National Meteorological Library on loan, if required.

1. **Research strategy and programme**
   K A Browning et al
   January 1993

2. **The GEWEX Cloud System Study (GCSS)**
   GEWEX Cloud System Science Team
   January 1993

3. **Evolution of a mesoscale upper tropospheric vorticity maximum and comma cloud from a cloud-free two dimensional potential vorticity anomaly**
   K A Browning
   January 1993

4. **The global energy and water cycle**
   K A Browning
   July 1993

5. **Structure of a midlatitude cyclone before occlusion**
   K A Browning and N Roberts
   July 1993

6. **Developments in systems and tools for weather forecasting**
   K A Browning and G Szejwach
   July 1993

7. **Diagnostic study of a narrow cold frontal rainband and severe winds associated with a stratospheric intrusion**
   K A Browning and R Reynolds
   August 1993

8. **Survey of perceived priority issues in the parametrizations of cloud-related processes in GCMs**
   K A Browning
   September 1993

9. **The effect of rain on longwave radiation**
   I Dharssi
   September 1993

10. **Cloud microphysical processes - a description of the parametrization used in the large eddy model**
    H Swann
    October 1993

11. **An appreciation of the meteorological research of Ernst Kleinschmidt**
    A J Thorpe
    May 1992

12. **Potential vorticity of flow along the Alps**
    A J Thorpe, H Volkert and Dietrich Heimann
    August 1992

13. **The representation of fronts**
    A J Thorpe
    January 1993

14. **A parametrization scheme for symmetric instability: test for an idealised flow**
C S Chan and A J Thorpe
February 1993

15. **The Fronts 92 Experiment: a Quicklook Atlas**
Edited by T D Hewson
November 1993

16. **Frontal wave stability during moist deformation frontogenesis**
Part 1: Linear wave dynamics
C H Bishop and A J Thorpe
May 1993

17. **Frontal wave stability during moist deformation frontogenesis**
Part 2. The suppression of non-linear wave development
C H Bishop and A J Thorpe
May 1993

18. **Gravity waves in sheared ducts**
S Monserrat and A J Thorpe
October 1993

19. **Potential vorticity and the electrostatics analogy: quasi-geostrophic theory**
C Bishop and A J Thorpe
November 1993

20. **Recent advances in the measurement of precipitation by radar**
A J Illingworth
April 1993

21. **Micro-physique et givrage: cloud microphysics and aircraft icing**
A J Illingworth
May 1993

22. **Differential phase measurements of precipitation**
M Blackman and A J Illingworth
May 1993

23. **Estimation of effective radius of cloud particles from the radar reflectivity**
N I Fox and A J Illingworth
May 1993

24. **A simple method of Dopplerising a pulsed magnetron radar**
A Hua, A J Illingworth and J Eastment
November 1993

25. **Radiation and polar lows**
George C Craig
February 1994

26. **Collected preprints submitted to the International Symposium on the Life Cycles of Extratropical Cyclones; Bergen, Norway, 27 June - 1 July 1994**
April 1994

27. **Convective frontogenesis**
Douglas J Parker and Alan J Thorpe
April 1994

28. **Improved measurement of the ice water content in cirrus using a total water evaporator**
Philip R A Brown and Peter N Francis
April 1994

29. **Mesoscale effects of a dry intrusion within a vigorous cyclone**
K A Browning and B W Golding
April 1994

30. **GEWEX Cloud System Study, Science Plan**
May 1994

31. **Parametrization of momentum transport by convectively generated gravity waves**
R Kershaw
May 1994

32. **Mesoscale Modelling Newsletter No 5**
May 1994

33. **Observations of the mesoscale sub-structure in the cold air of a developing frontal cyclone**
K A Browning, S A Clough, C S A Davitt, N M Roberts and T D Hewson
May 1994

34. **Longwave radiative forcing of a simulated tropical squall line**
Imtiaz Dharssi
July 1994

35. **On the nature of the convective circulation at a kata-cold front**
K A Browning
September 1994

36. **Collective preprints of papers submitted to the COST-75 International Seminar on Advanced Weather Radar Systems, Brussels, 20-23 September 1994**
November 1994

37. **Use of satellite imagery to diagnose events leading to frontal thunderstorms: Parts I and II of a case study**
K A Browning and N M Roberts
November 1994

38. **The role of spaceborne millimetre-wave radar in the global monitoring of ice cloud**
P R A Brown, A J Illingworth, A J Heymsfield, G M McFarquhar, K A Browning and M Gosset
December 1994

39. **Potential vorticity inversion**
Michal Ziemianski
October 1994

40. **Theory of mature tropical cyclones; a comparison between Kleinschmidt (1951) and Emanuel (1986)**
Suzanne L Gray
December 1994

41. **Dispersion and removal of pollutants during the passage of an atmospheric frontal system**
N R Gimson
December 1994

42. **The role of snow sublimation in frontogenesis**
D J Parker and A J Thorpe
December 1994

43. **Potential vorticity and the electrostatics Analogy: Ertel-Rossby formulation**
A J Thorpe and C H Bishop
December 1994

44. **Mesoscale aspect of extratropical cyclones: an observational perspective**
K A Browning
January 1995

45. **A polar low outbreak: evolution and mesoscale structures**
T D Hewson, G C Craig and C Claud
February 1995

46. **Generation of near-surface gusts of deep convection**
K Nakamura and R Kershaw
April 1995

47. **Attribution concepts applied to the Omega Equation**
S A Clough, C S A Davitt and A J Thorpe
June 1995

48. **Parametrization of mixed-phase cloud and precipitation**
Susan P Ballard and M Gerard Hutchinson
June 1995

49. **Short-range forecasting of stratocumulus: initialization prediction**
Susan P Ballard, Simon D Jackson and B Macpherson
June 1995

50. **Contributions of the JCMM/Dept of Meteorology Radar Group to the 27th AMS Radar Meteorology Conference, Vail October 1995**
June 1995

51. **Cold pools in shear**
Douglas J Parker
September 1995

52. **High-resolution analysis of frontal fracture**
K A Browning, S P Ballard and C S A Davitt
September 1995

53. **The albedo of broken cloud fields: calculations using a modified two stream radiation code**
Imtiaz Dharssi and Roy Kershaw
October 1995

54. **Parametrization of momentum transport by convection. I: theory and cloud modelling results**
R Kershaw and D Gregory
November 1995

55. **Variation of frontal structure along a cold front**
K A Browning and N M Roberts
November 1995

56. **Secondary frontal waves**
Douglas Parker
December 1995

57. **Objective fronts**
T D Hewson
March 1996

58. **Mesoscale analysis of the activation of a cold front during cyclogenesis**
K A Browning, N M Roberts and A J Illingworth
June 1996

59. **Investigation of different representations of rain in a 1-d evaporation model**
H Swann
May 1996

60. **Parametrization of diabatic processes in the inversion of the omega-equation**
M Athanassiadou and A J Thorpe
June 1996

61. **The role of the environmental flow in the development of secondary frontal cyclones**
I A Renfrew, A J Thorpe and A Joly
June 1996

62. **Consequences of the geostrophic momentum approximation on barotropic instability**
S Malardel, A J Thorpe and A Joly
June 1996

63. **Contributions to the AMS/RMS Conference on Mesoscale Processes**
Reading, 9-13 September 1996

64. **Vorticity and potential vorticity in stratified flows interacting with an isolated obstacle**
Jorge A Gutiérrez and A J Thorpe
September 1996

65. **Triple point development: two case studies**
Douglas Parker
September 1996

66. **Radar observations of wind-shear splitting within evolving atmospheric Kelvin-Helmholtz billows**
D Chapman and K A Browning
April 1997

67. **Cold frontal structure derived from radar wind profilers**
K A Browning, D Jerrett, J Nash, T Oakley and N M Roberts
May 1997

68. **The dry intrusion and its effect on the frontal, cloud and precipitation structure of extratropical cyclones**
K A Browning - Text of invited special lecture at the Spring Conference
of the Meteorological Society of Japan, University of Tsukuba, 22 May 1997

69. **Met. Office Unified Model data, diagnostics, graphics programs, and other observational data available from the JCMM through the aegis of the Universities Weather Research Network (UWERN).** (Plus supplement)
Peter Panagi and Ed Dicks
June 1997

70. **Contributions of the JCMM/Dept of Meteorology Radar Group to the 28th AMS Radar Meteorology Conference.** Austin, Texas
September 1997

71. **Sensitivity of short-range weather forecasts to local potential vorticity modifications**
Meral Demirtas and Alan Thorpe
July 1997

72. **Objective identification of frontal wave cyclones**
T D Hewson
August 1997

73. **Attribution and its application to mesoscale structure associated with tropopause folds**
A J Thorpe
September 1997

74. **The role of the environmental flow in the development of secondary frontal cyclones**
Ian A Renfrew, Alan J Thorpe and Craig H Bishop
September 1997

75. **Potential vorticity: a short history of its definitions and uses**
Alan J Thorpe and Hans Volkert
September 1997

76. **Superposing semi-geostrophic potential vorticity anomalies**
H R Birkett and A J Thorpe
September 1997

77. **Short period forecasting of catchment-scale precipitation.**
Part 1: the role of Numerical Weather Prediction
M A Pedder, M Haile and A J Thorpe
September 1997

78. **Verification of the tracking technique used in an experimental cloud motion wind inferring system**
Z Wang, K A Browning and G A Kelly
October 1997

79. **A preliminary study of Fourier series analysis for cloud tracking with GOES high temporal resolution images**
Z Wang
October 1997

80. **Analysis of an ex-tropical cyclone after reintensifying as a warm-core extratropical cyclone**
K A Browning, G Vaughan and P Panagi
November 1997

81. **A JCMM overview of FASTEX IOPs**
S A Clough, H W Lean, N M Roberts, H Birkett, J-P Chaboureau, R Dixon,
M Griffiths, T D Hewson and A Montani
January 1998

82. **Programs for PV inversion and modification**
Meral Demirtas
December 1997

83. **Release of potential shearing instability in warm frontal zones**
D Chapman and K A Browning
February 1998

84. **The European Cloud-Resolving Modelling Programme (EUCREM)**
Summary Report from the coordinator
P W White
April 1998

85. **A frontal wave database**
T D Hewson
April 1998

86. **Layering observed in dropsoundings from IOP 1 of Fronts 92**
S A Clough
May 1998

87. **Use of wind-shear displays for Doppler radar data**
D Chapman and K A Browning
May 1998

88. **Radar estimates of rainfall rates at the ground in bright band and non-bright band events**
T J Smyth and A J Illingworth
June 1998

89. **Correction for attenuation of radar reflectivity using polarisation data**
T J Smyth and A J Illingworth
June 1998

90. **The effects of convection on chemical reactions and precipitation scavenging**
Neil R Gimson
July 1998

91. **How to use the display program DISP**
Nigel Roberts
August 1998

92. **Conceptual models of cyclogenesis**
Adrian T Semple
August 1998

93. **Observations of oblate hail using dual polarisation radar and implications for hail detection schemes**
T J Smyth, T M Blackman and A J Illingworth
September 1998

94. **The semigeostrophic diagnosis of vertical motion. Part I: Formulation and co-ordinate transformations**
Mike A Pedder and Alan J Thorpe
September 1998

95. **The semigeostrophic diagnosis of vertical motion. Part II: Results for an idealised baroclinic wave life cycle**
Alan J Thorpe and Mike A Pedder
September 1998

96. **Convective destabilisation by a tropopause fold diagnosed using potential vorticity inversion**
Morwenna Griffiths, Alan Thorpe and Keith Browning
October 1998

Met Office Joint Centre for Mesoscale Meteorology Department of Meteorology
University of Reading PO Box 243 Reading RG6 6BB United Kingdom
Tel: +44 (0)118 931 8425 Fax: +44 (0)118 931 8791
www.metoffice.com